

Modeling the Geometry of Satin Weave Fabric Composites

M. P. RAO,[†] M. PANTIUK AND P. G. CHARALAMBIDES*

*Department of Mechanical Engineering, The University of Maryland
Baltimore County, 1000 Hilltop Circle, Baltimore, MD 21250, USA*

ABSTRACT: The focus of this study is aimed at characterizing the weave architecture in orthogonally woven polymer and ceramic–matrix composites. Three-dimensional (3D) geometric models of the unit-cells of four harness (4HS), five harness (5HS), and eight harness (8HS) satin weave morphologies are developed. The fiber bundle and matrix architecture in the 4HS, 5HS, and 8HS morphologies is represented via mathematical shape functions within the domain of the repeating unit-cells of the woven fabrics. This work brings together the non-uniform layer methodology of Kuhn and Charalambides [1] and the sub-cell modeling approach developed by Hewitt et al. [2]. In addition, this article introduces the novel concept of a ‘middle matrix layer’ in capturing the ingress of matrix material away from undulating bundle regions, as documented by Morscher [3]. The geometry models developed herein account for a porous polymer matrix deposited over the woven mat via either resin film infusion (RFI) or resin transfer molding (RTM). This modeling also incorporates micro-structural intricacies observed in woven CMCs fabricated using chemical vapor infiltration (CVI) techniques for the deposition of the ceramic–matrix phase. Finally, results on the overall volumetric composite characteristics are reported.

KEY WORDS: surface functions, geometric modeling, finite elements, discretization, composites, fiber, bundles, unit-cell, volume fraction.

INTRODUCTION

WOVEN FABRIC COMPOSITES are being considered as viable alternatives to monolithic materials in a wide range of specialized applications. However, their successful use is limited by our ability to effectively characterize their complex micro-structure and associated macro-mechanical failure response. Thus, the development of detailed and robust geometric models (see Ref. [1]) that capture the intricate complex micro-structural characteristics of the woven systems is of critical importance.

Kuhn and Charalambides [1] developed a new class of mathematically piecewise continuous shape functions in describing the geometry of fiber bundles in plain weave

[†]Present address: Department of Mech. and Aero. Engg., University of Florida, FL 32611, USA, Gainesville.

*Author to whom correspondence should be addressed. E-mail: panos@umbc.edu

Figures 3–6, 8, 14 and 17 appear in color online: <http://jcm.sagepub.com>

fabric composites. Formulations for the presence of large scale macroscopic voids often observed in the matrix phase are also developed.

In studies reported elsewhere [4–7], researchers have developed geometry models to characterize the micro-structural complexities often observed in woven fabric composites. In Ref. [4], the methodology of describing the geometry of the woven unit cell relies on characterizing the centerline of each fiber bundle (tow) as a Bezier curve, interpolating a set of discrete control points and then sweeping the cross-section of the tows over this curve, to generate a continuous tow.

Raju et al. [8] presented several two-dimensional (2D) renditions of PW, 5HS, and 8HS satin weave composites with a view to extract the repeating unit cells (RUCs) and further develop three-dimensional (3D) models of these RUCs. However, the level of detail incorporated in that geometric modeling effort was rather simplistic as the fiber bundle cross-sections were assumed to be rectangular and the bundles were assumed to undulate only in the gap or bridge region between orthogonal fiber tows. Micrographs of the Nicalon™ fiber reinforced CVI SiC plain weave composite presented in Ref. [1] suggest that the fiber tow path continuously undulates and that the fiber tow cross-section is more elliptical than rectangular. In addition to the above-mentioned geometry simplification the model developed in Ref. [8] was also limited to describing a fully dense matrix material surrounding the fiber tows while the presence of discrete matrix voids in porous matrix fabric composites was not addressed.

The geometric modeling methodology employed in this study is similar to that employed by previous researchers [2,8–11]. In particular, the techniques employed herein are inspired by the methodology developed by Hewitt et al. [2]. In that study, the authors compiled a library of 32 sub-cells incorporating various domains of fiber bundle undulation, which were then assembled in accordance with a weave point diagram established for each type of weave. Hewitt et al. [2], assumed the fiber bundle cross-sections to be somewhat square and modeled undulating profiles of the fiber tows with appreciable discontinuities. In addition, the model presented in Ref. [2] does not incorporate the complex geometry of the matrix material surrounding the fiber tows. This work aims at developing a robust library of mathematical models capable of capturing the intricate details of an entire class of satin weave systems.

The geometry modeling and characterization presented herein establish the critical modeling framework for broad thermo-mechanical studies using the method of finite elements. As such, the validation of FE models is not central to this study and is addressed elsewhere [12] as well as in complementary studies now in progress. The general methodology employed in this study shall be presented next.

AN OVERVIEW OF THE GEOMETRIC MODELING METHODOLOGY

In order to model the geometry of inherently complex material systems such as satin weave composites, it is essential to understand the details of their intricate micro-structural architecture. The architecture of satin woven morphologies is characterized by undulating as well as straight non-undulating segments of the woven fiber tows, as evident schematically in Figure 1 wherein a cross-sectional profile of a 5HS system is shown. Similar geometric features of undulating and straight tow segments are exhibited in the 4HS and 8HS systems. Unlike the above morphologies, plain weave morphologies exhibit continuously undulating tows as shown in Figure 2.

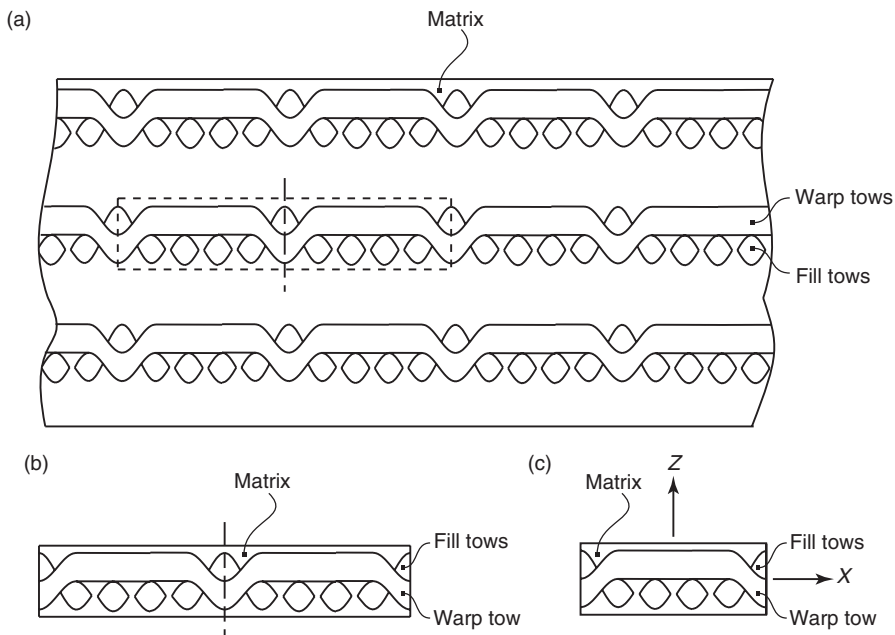


Figure 1. Schematic representation of the cross-section of a five harness woven laminate. (a) Identification of the full representative unit-cell. (b) Detailed view of the full representative unit-cell showing the fiber tows and matrix material. (c) The schematic representation of the basic or repeating unit cell (RUC).

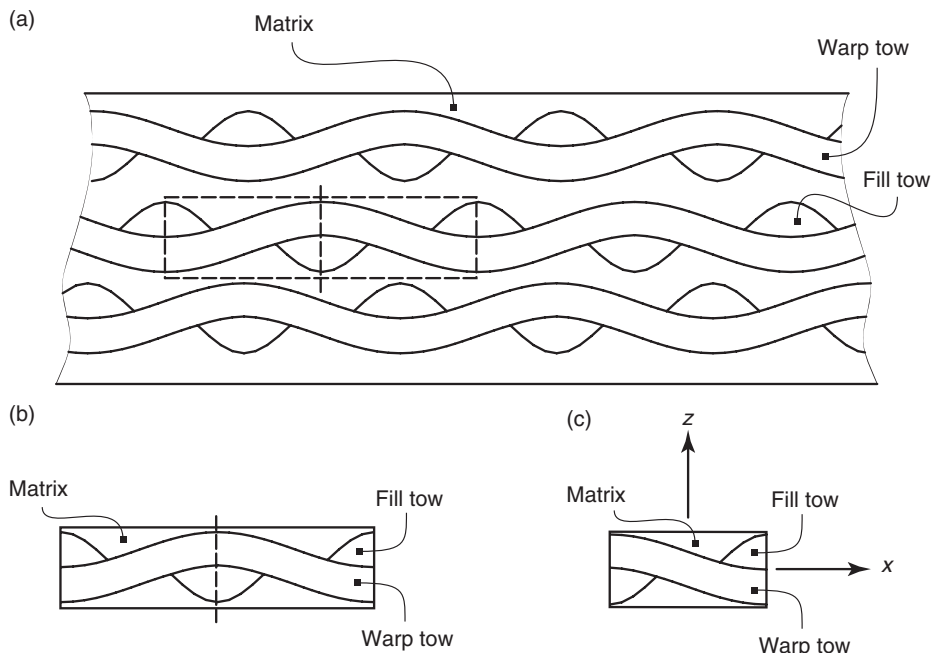


Figure 2. Schematic representation of the cross-section of a plain woven laminate. (a) Identification of the repeating unit cell (RUC). (b) Detailed view of the RUC showing the fiber tows and matrix material. (c) The schematic representation of the symmetric part of the RUC.

A novel contribution of this geometric modeling work is the introduction of a ‘middle matrix layer’ as the region bounded by the interior spatially varying region between the upper and lower fiber bundles in the 4HS, 5HS, and 8HS systems. As such, this ‘middle matrix’ region is purely auxiliary and critical to the robustness of the respective geometric models. Careful examination of the micrographs reported in Ref. [3] reveals evidence of the matrix ingress represented through the ‘middle matrix layer’ incorporated in the geometry models reported in this work.

As shown in Figures 1 and 2, the micro-structures of plain as well as satin woven fabric composites are complex. Additionally, in satin weave fabric composites, the domain of the RUC encompasses as many fiber tows as the minimum loom harness number (N_g) [8] of the particular weave. Therefore, as shown in Figure 1, the RUC for a five harness (5HS) satin weave envelopes five (5) warp fiber tows and five (5) fill fiber tows. Similarly it could be envisioned that the RUC of a 4HS fabric composite would envelope four (4) warp fiber tows and four (4) fill fiber tows, while the RUC of the 8HS fabric composite would encompass eight (8) warp as well as fill fiber tows. Schematic and 3D finite element representations of the PW, 4HS, 5HS, and 8HS satin weave fabric composites shown in Figure 3 bring to light the underlying fundamental weave patterns in these complex material systems. The main focus of this study is to develop mathematical surface functions for the tow and matrix phases for each of the woven geometries shown in Figure 3. The above functions would then be integrated into parametric meshing schemes as needed to develop requisite finite element meshes for the plain and satin weave systems.

The first step in the geometric modeling of these material systems requires the characterization of the bounds of the geometrically repeating unit-cell of each woven morphology from within the 2D woven mat. Mathematical shape functions would be developed in the following sections to describe the fiber tow and matrix layer geometry within the domain of these RUCs. By closer inspection of the 5HS system, one can establish that the unit-cell itself comprises of five binary geometric domains, as shown in Figure 4(a). These repeating geometric domains would be referred to in this work as ‘binary sub-cells’. The 3D finite element mesh of the fiber tow architecture within the basic or repeating unit-cell of the 5HS woven system is reported in Figure 4(b).

A schematic representation of the imprints of the fiber tow architecture in the four and eight harness satin weaves highlighting the domains of the RUCs are presented in Figure 5(a) and (b), respectively. As shown in Figure 5(c), the same binary sub-cells associated with the 5HS system can also be used to construct the 4HS and 8HS systems as well. For the 4HS fabric though, we need three of the binary sub-cells viz., sub-cell nos. 1, 4, and 5 from the 5HS repeating unit-cell whereas an additional binary sub-cell no. 6 needs to be defined. In all, we developed a library of six binary sub-cells which were assembled using a parametric scheme to generate the 3D finite element definitions of the basic or repeating unit-cells of the 4HS, 5HS, and 8HS woven fabric composites. The top views of the individual binary sub-cells formulated in this study are shown in Figure 5(c).

The corresponding 3D isometric views of the fiber tow architecture and matrix layer geometry captured within the individual binary sub-cells are reported in Figure 6. In particular, we develop mathematical surface functions to spatially describe the fiber tow and matrix layer geometry in binary sub-cell no. 1. Then via suitable reflections of these surface functions we characterize the fiber tow undulation and spatial variation of the

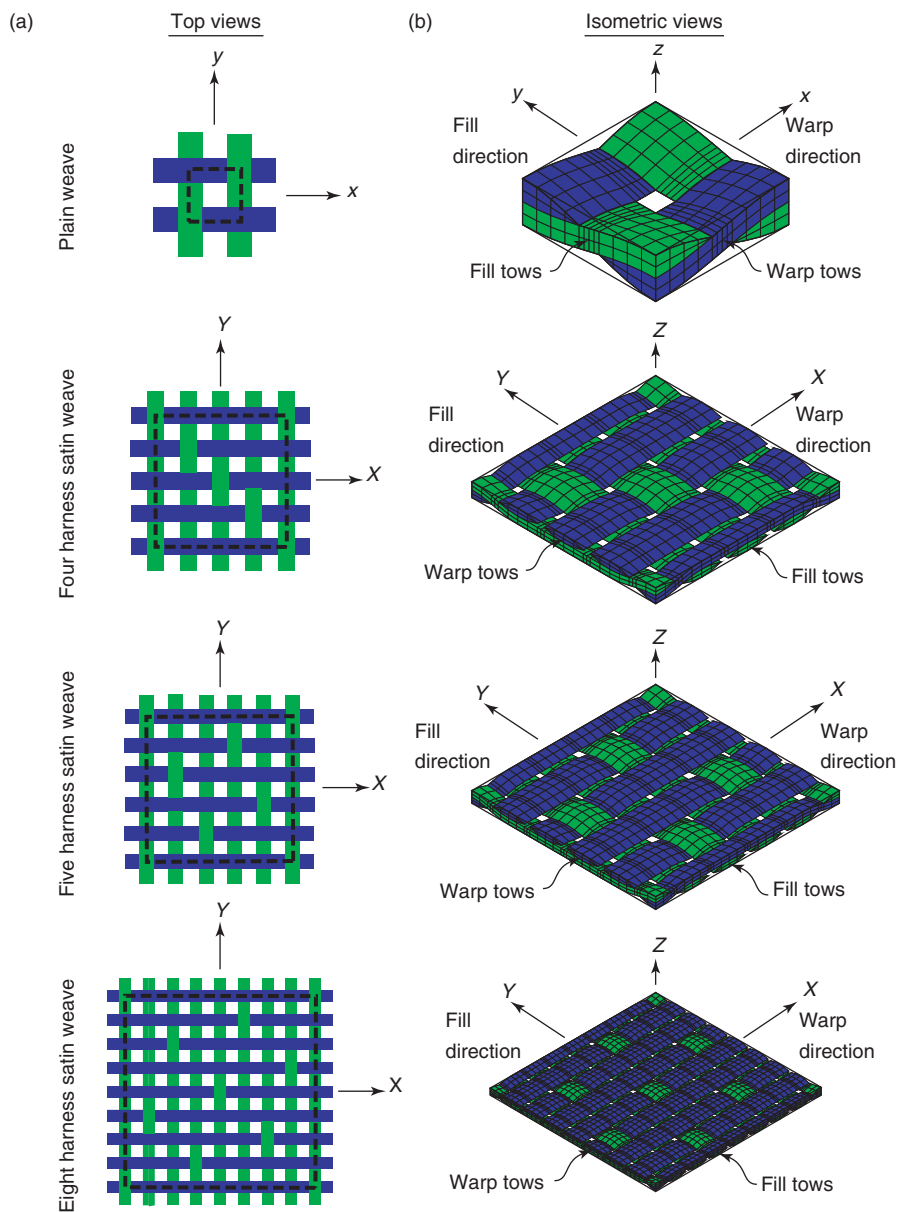


Figure 3. Schematic and finite element representations of the symmetric unit-cell of the plain weave system and the RUCs of the satin weave fabric architectures. Column:(a) Top views of the weave patterns showing the bounds of the symmetric unit-cell in the plain weave and the RUCs in the satin weave systems. Column:(b) Three-dimensional (3D) finite element discretizations of the symmetric unit-cell of the plain weave and the RUCs of the 4HS, 5HS, and 8HS satin weave systems.

matrix layer in binary sub-cell nos. 2 through 4. Binary sub-cell no. 5 captures the straight and non-undulating domains of the fiber tows in the satin weave fabrics. As such, a very simple mathematical function is used to describe the fiber tow architecture in this binary sub-cell as would be discussed in the following sections. Finally, the binary sub-cell no. 6 is

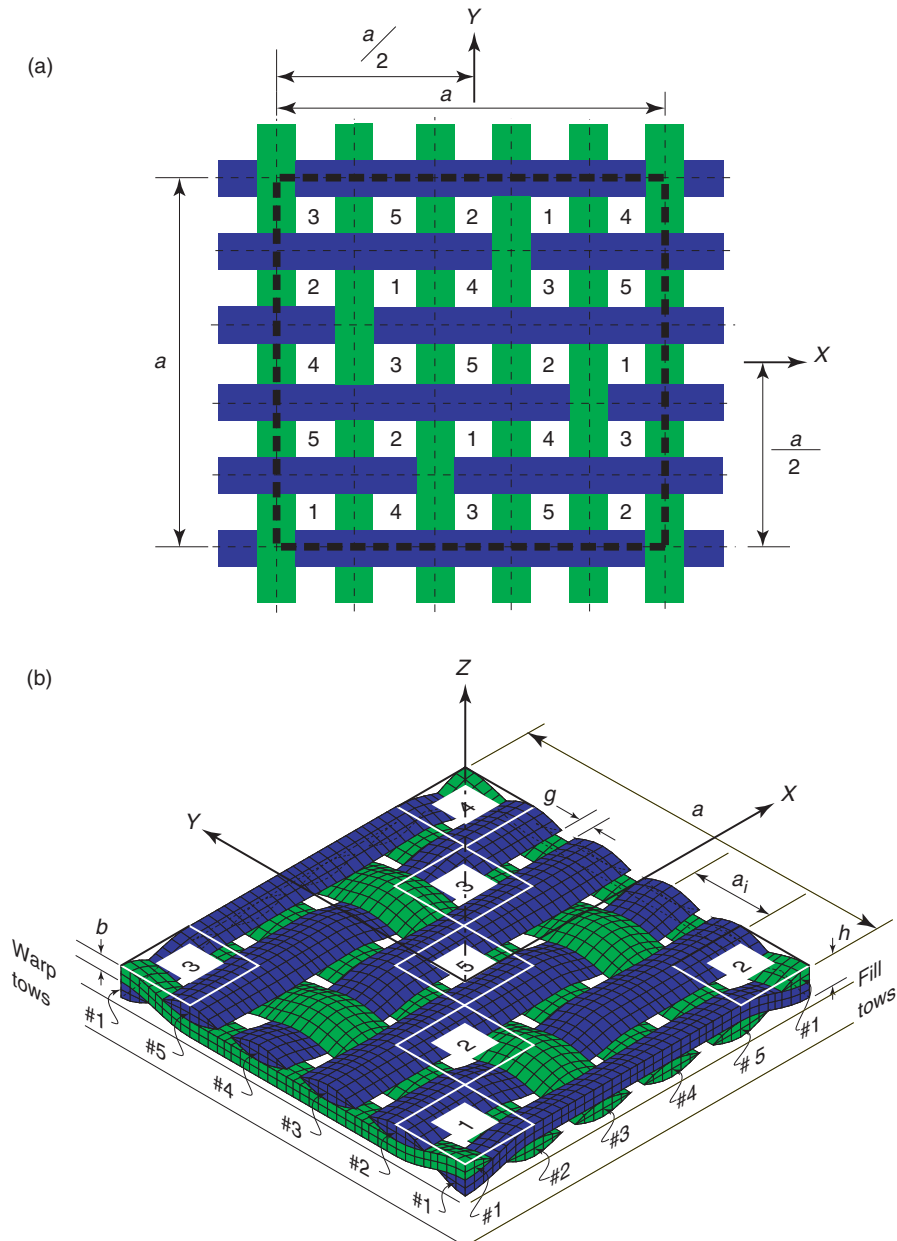


Figure 4. (a) Top view of the RUC of the 5HS woven system. The numbers within each square region indicate the type of binary sub-cell occupying that location. (b) An isometric view of the corresponding 3D finite element mesh of the 5HS weave pattern shown in (a). For clarity, only few locations of the individual binary sub-cells are shown in (b).

derived from the PW morphology through suitable geometric reflections of the corresponding PW fabric surface functions. These fundamental traits considerably simplify the challenging task of describing the micro-structural geometry of satin weave polymer and ceramic matrix fabric composites.

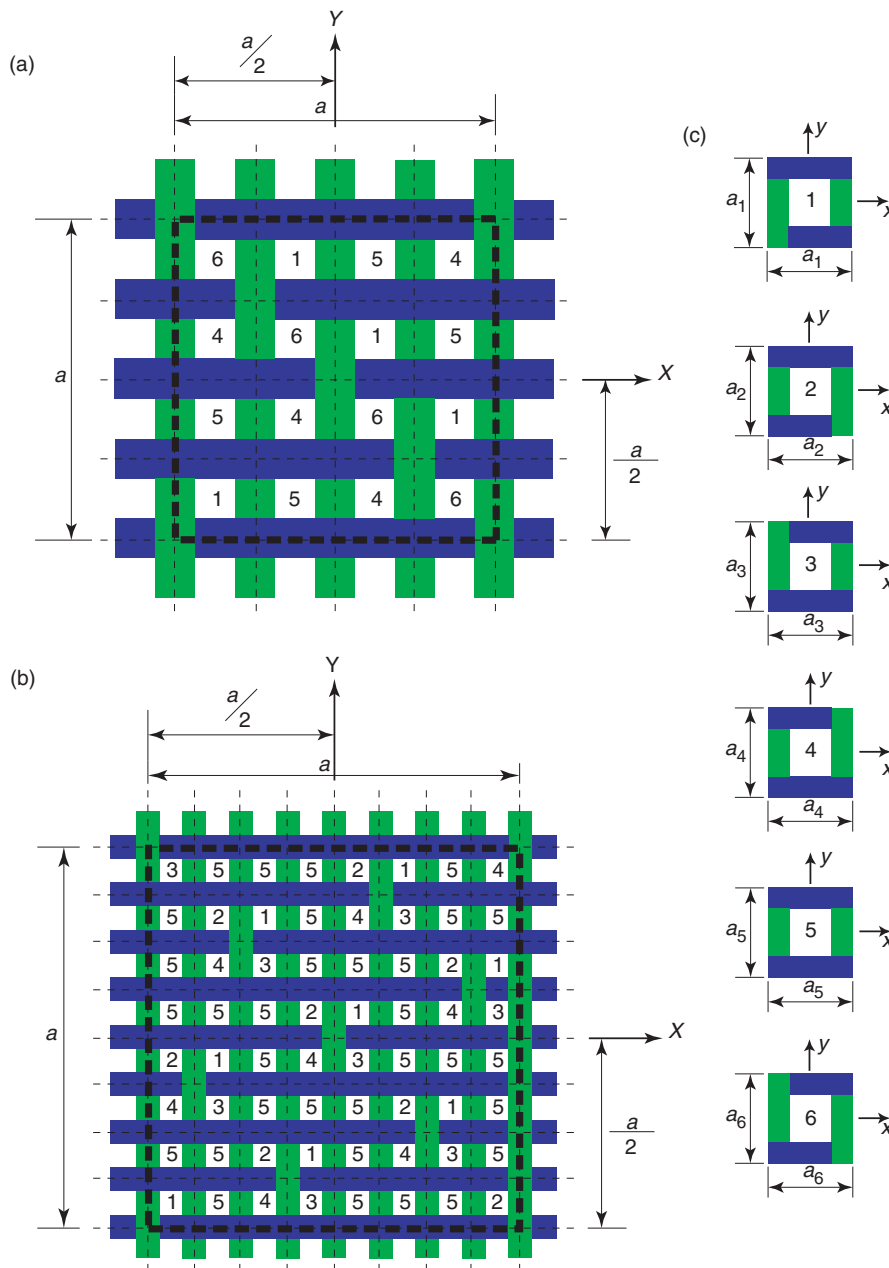


Figure 5. Top views of the RUCs. The numbers within dashed lines indicate the type binary sub-cell occupying that location. (a) The 4HS woven system. (b) The 8HS woven system. (c) The top view of each binary sub-cell used to assemble the 4HS and 8HS systems.

The mathematical surface functions developed in this study are defined relative to the local xyz coordinate system of the binary sub-cells that are translated to the appropriate location relevant to the global XYZ coordinate system of the basic or repeating unit-cell of the particular weave. As such, the orientation of the local xyz coordinate systems in

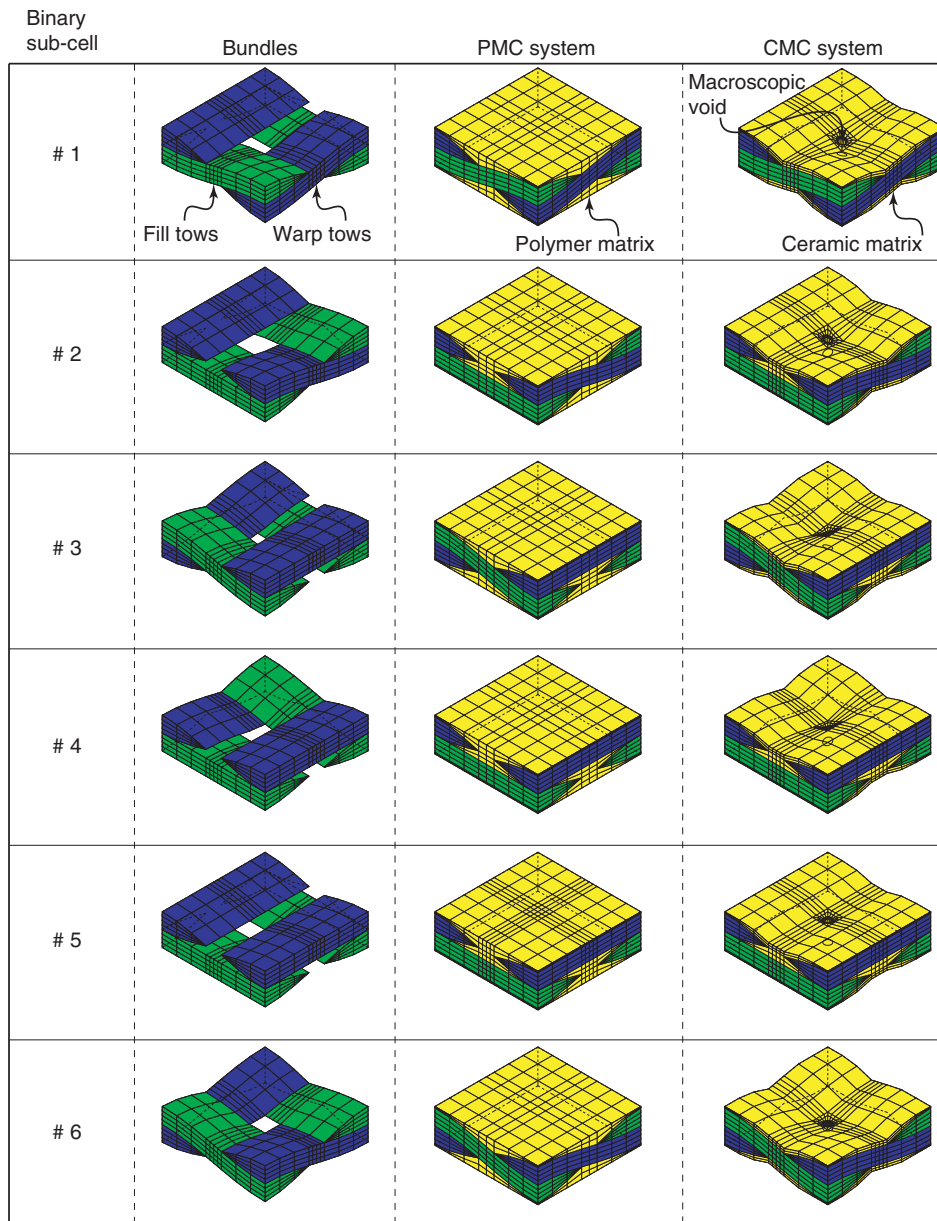


Figure 6. The library of binary sub-cells developed in this study. The left column of meshes represents the fiber bundle architecture captured in each binary sub-cell. The middle column of meshes displays the polymer matrix composite (PMC) model whereas the right column of meshes incorporates large-scale matrix voids used in modeling ceramic matrix composites (CMCs).

individual binary sub-cells are defined to be parallel to the global XYZ coordinate system of the basic or repeating unit-cell. However, the origin of the xyz coordinate system in every binary sub-cell is located at the geometric center of the i th sub-cell of dimensions $a_i \times a_i \times h$ as depicted in Figure 7. The choice of the particular functional forms representing the tow

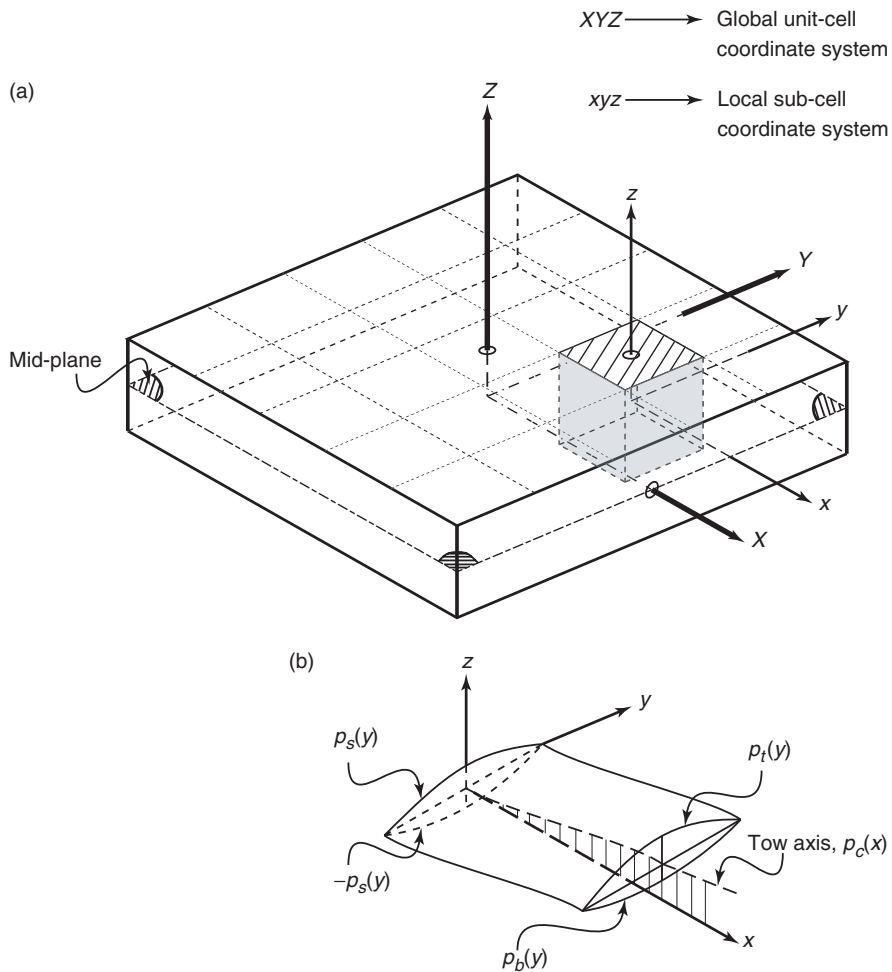


Figure 7. Mapping between the local binary sub-cell xyz and global unit-cell XYZ coordinate systems. The mathematical representations of the tow edge profiles and centroidal tow axis are first developed with respect to the local coordinate system xyz .

centroidal and cross-sectional profiles shown in Figure 7 will be discussed in the following section and is based on the work of Kuhn and Charalambides [1].

FIBER BUNDLE AND MATRIX SURFACE FUNCTIONS IN BINARY SUB-CELL NO. 1

The general class of mathematical surface functions developed in this study are inspired by the works of Kuhn and Charalambides [1], Whitcomb et al. [13] and Whitcomb and Tang [14]. In Refs [13] and [14], the details regarding the methodology of finite element discretization were not addressed. Also in those studies, the finite element discretization did not account for the presence of large matrix voids that have been known to influence the microscopic stress fields in the matrix layer [15–18]. As such, the new class of

mathematical shape functions developed in the present study builds on the work presented by Kuhn and Charalambides [1] wherein the presence of large matrix voids is modeled.

Porous Matrix Model for the Binary Sub-Cell No. 1

Details of the binary sub-cell no. 1 are shown in Figure 8 where the fiber tow architecture is represented as the warp and fill tow layers. The dotted line in the gap region between the tows represents a special function employed to fully describe the top and bottom surfaces of the individual tow layers everywhere within the domain of the binary sub-cell no. 1. Along with the tows, a fully dense *soft*-polymer matrix material is modeled

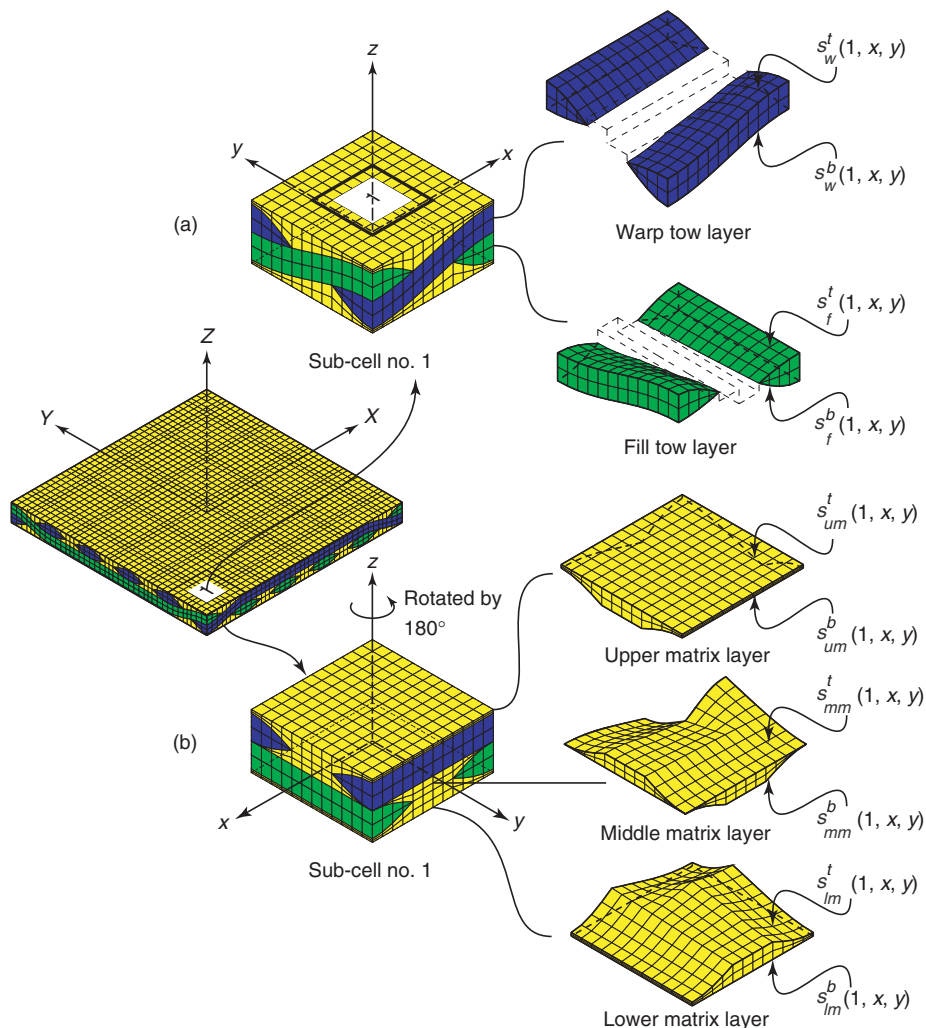


Figure 8. Geometric details of the binary sub-cell no. 1 depicting scaled-up isometric views of individual layers. The architecture of the novel middle matrix layer introduced to characterize the geometry of the material is also shown.

to surround the tows. As discussed earlier in this study, the novel concept of a ‘middle matrix layer’ is introduced as an effective means of capturing the spatially varying interior region observed in satin weaves. Thus, the mathematical description of the matrix material is prescribed in terms of three individual layers, i.e., the upper matrix layer, the middle matrix layer and the lower matrix layer, as shown in Figure 8.

The overall dimensions of the repeating unit-cell of the 5HS woven fabric are $a \times a \times h$, consistent with Figure 4(b). The schematic representation of a single ply of 5HS woven fabric detailing the various geometry parameters and delineating different material components is presented in Figure 9. The in-plane length and also the width of the unit-cell is designated a as shown in Figure 9, while h is used to represent the overall height of the ply. The gap between parallel tows is identified by the variable g while the in-plane dimensions of each binary sub-cell combining to form the 5HS woven unit-cell is accorded the symbol a_i . The maximum thickness of the tows is assigned the variable b .

The sinusoidal waveform assumed to describe the centroidal path of the undulating tows with respect to the local xyz coordinate system of the binary sub-cell no. 1 is given by:

$$p_c(x) = \sin\left(\frac{\pi x}{a_1}\right). \tag{1}$$

A similar functional form can be used to represent the centroidal path of the undulating fill tows in the orthogonal direction by replacing the parameter x with the parameter y and changing the sign in front of the sine function in Equation (1) as required. Referring to the schematic of the undulating fiber tow in Figure 7, the bottom edge profile of the tow p_b is modeled to have the same functional form as the centroidal tow in order to maintain contact and is given by:

$$p_b(x) = \sin\left(\frac{\pi x}{a_1}\right). \tag{2}$$

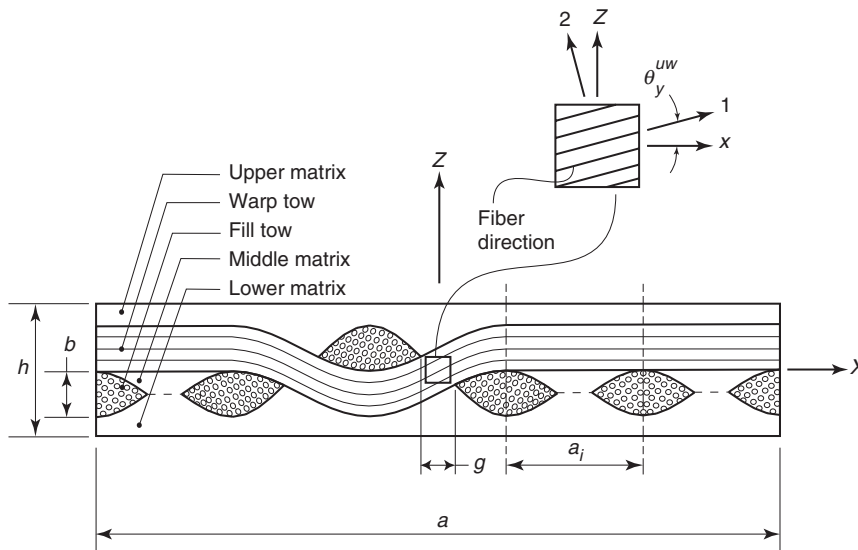


Figure 9. Geometry parameters employed in the porous matrix model.

The large amplitude top edge profile p_t of the tow cross-section shown in Figure 7 is given by:

$$p_t(x) = (1 + \beta) \sin \left[\frac{\pi}{a_1 - g} (x - \text{sign}(x)g/2) \right] - \text{sign}(x)\beta \quad (3)$$

where:

$$\beta = \sin \left(\frac{\pi g}{2a_1} \right) \quad (4)$$

and the discontinuous sign function is defined in Ref. [1]:

$$\text{sign}(x) = \begin{cases} -1 & x < 0 \\ +1 & x \geq 0. \end{cases} \quad (5)$$

The symmetric profile of the tow cross-section as illustrated in Figure 7 is given by:

$$p_s(x) = \sin \left[\frac{\pi}{a_1 - g} (x - \text{sign}(x)g/2) \right]. \quad (6)$$

The cross-sectional profiles defined in Equations (2) and (3) would be used to develop the shape functions describing the tow architecture in binary sub-cell no. 1 as shown in Figure 8. Note that in binary sub-cell no. 1, the warp tow undulates in the domain $-a_1/2 \leq x \leq a_1/2$ and $y < -g/2$, while in the domain $-a_1/2 \leq x \leq a_1/2$ and $y > g/2$ the tow is straight and non-undulating. Similarly, the fill tow undulates in the domain $x < -g/2$ and $-a_1/2 \leq y \leq a_1/2$, while this tow remains straight in $x > -g/2$ and $-a_1/2 \leq y \leq a_1/2$. Consistent with the modeling techniques described in Ref. [1], treating each material component of the binary sub-cell no. 1 as an individual layer, the complex tow and matrix architecture could be represented via robust mathematical shape functions. In order to incorporate all the characteristics of the fiber tow undulation often observed in satin weave composite systems, we make use of an inherently discontinuous interpolation function:

$$R(x, y) = \begin{cases} \frac{x}{g} + \frac{1}{2} & |x| < g/2; \quad -a_1/2 \leq y \leq -g/2 \\ H(x) & g/2 \leq |x| \leq a_1 - g/2; \quad -a_1/2 \leq y \leq -g/2 \\ 0 & \text{otherwise} \end{cases} \quad (7)$$

where, the Heaviside step function is given by:

$$H(x) = \begin{cases} 0 & x < 0 \\ 1 & x \geq 0. \end{cases} \quad (8)$$

In an effort to generate the top surface of the undulating part of the warp tow in binary sub-cell no. 1, the centroidal path of the tow is assigned the functional form $p_c(x)$ from Equation (1) and the profile describing the top edge of transverse section of the tow is

summed with $p_c(x)$. The top surface of the undulating part of the warp tow is characterized by the profile p_b in the interlace region bounded by $x < 0$ and $y < 0$, whereas in the line contact region defined by $x > g/2$ and $y < 0$ the top surface of the tow cross-section has the profile p_s . Therefore, p_b is multiplied by the ramp function $R(x, y)$ and summed with $p_c(x)$. In both of the two regions described above, the ramp function assumes the value of 1 and as such, the transverse profile remains unaltered. However, in the bridge region categorized by $|x| < g/2$ and $y < 0$, the ramp function linearly varies from 1 to 0, which when reversed and multiplied by the profile p_s gives rise to a linear interpolation between p_b and p_s in the bridge region. The top surface of the non-undulating part of the warp tow layer in the domain characterized by $-a_1/2 \leq x \leq a_1/2$ and $g/2 \leq y \leq a_1/2$ is modeled as a linear interpolation between p_t and p_s to account for the constraint imposed by the undulating fill tow on the non-undulating part of the warp tow as shown in Figure 8.

The characteristics of the top surface of the undulating part of the warp tow shown in Figure 8 and described above are mathematically realized by assembling Equation (1)–(7) in the following manner:

$$s_{t1}(x, y) = -\frac{b}{2}(\text{sign}(y)p_c(x) + R(\text{sign}(y)x, y)p_b(y) + R(-\text{sign}(y)x, y)p_s(y)) \quad (9)$$

in:

$$-\frac{a_1}{2} \leq x \leq \frac{a_1}{2} \quad \text{and} \quad y \leq -\frac{g}{2}$$

Equation (9) plotted as a surface is shown in Figure 10(a). In a similar manner, the geometric details of the non-undulating part of the warp tow are addressed by the following mathematical relationship:

$$s_{t2}(x, y) = -\frac{b}{2}(R'(-x)p_t(y) + R'(x)p_s(y)) \quad (10)$$

where the linear interpolation function $R'(x)$ is defined in the domain $-a_1/2 \leq x \leq a_1/2$ and $g/2 \leq y \leq a_1/2$ as:

$$R'(x) = \frac{x}{a_1} + \frac{1}{2}. \quad (11)$$

The surface plot of Equation (10) is reported in Figure 10(b). Equation (9) and (10) could then be combined to describe the top surfaces of the warp tow everywhere in the domain of the binary sub-cell no. 1 as follows:

$$s'_w(x, y) = \begin{cases} \frac{b}{2}[H(y) - F_H(y)\{H(-y)\text{sign}(y)p_c(x) + R(\text{sign}(y)x, y)p_b(y) \\ + R(-\text{sign}(y)x, y)p_s(y) - H(y)s_{t2}(x, y)\}] \end{cases} \quad (12)$$

in:

$$-\frac{a_1}{2} \leq x \leq \frac{a_1}{2} \quad \text{and} \quad -\frac{a_1}{2} \leq y \leq \frac{a_1}{2}$$

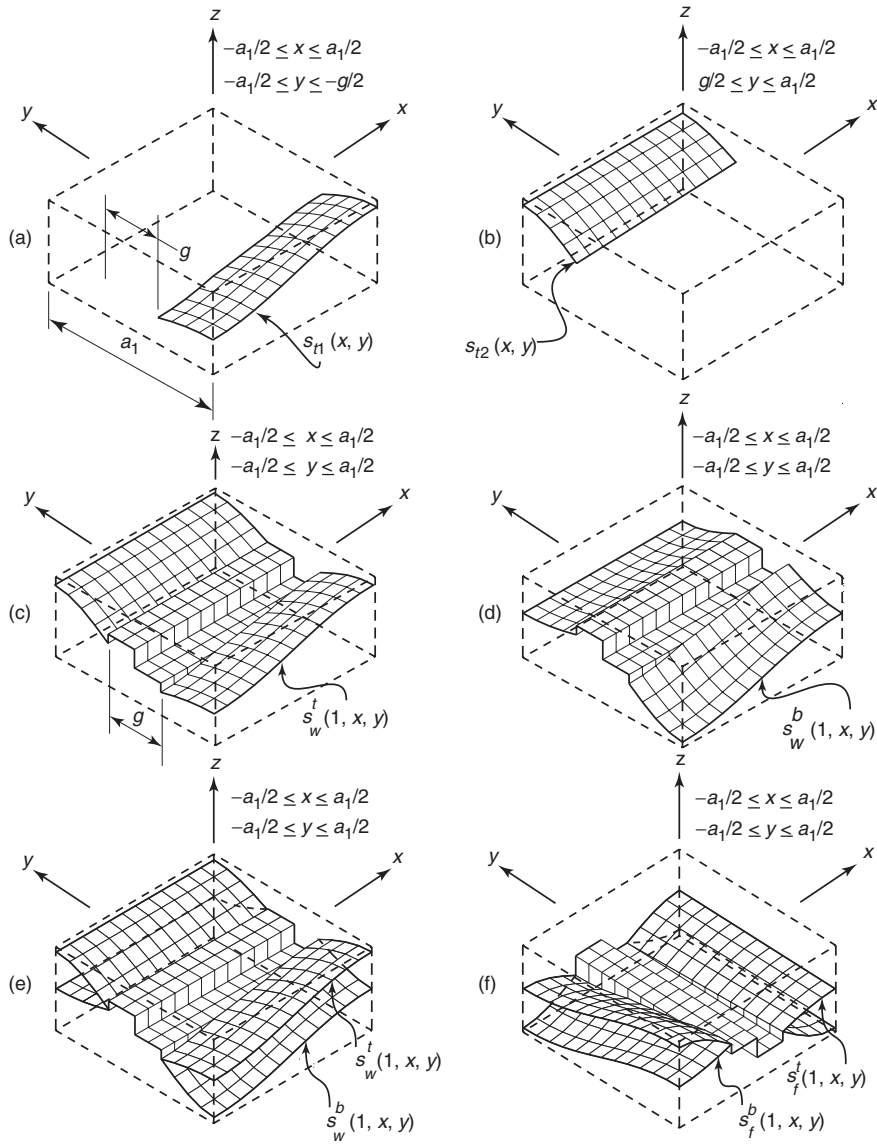


Figure 10. Geometric details of the fiber tow surfaces in binary sub-cell no. 1. (a) Undulating part of the top surface of the warp tow layer. (b) The straight non-undulating part of the top surface of the warp tow. (c) Top surface of the warp tow layer combining undulating and non-undulating domains of the warp tow layer. (d) Bottom surface of the warp tow layer. (e) The complete warp tow layer showing the top and bottom surfaces. (f) The complete fill tow layer showing the top and bottom surfaces.

where the function $F_H(x)$ is introduced to force the tow surface height to zero in all those regions where the tow does not exist. The function $F_H(x)$ has the following functional form:

$$F_H(x) = H\left(|x| - \frac{g}{2}\right) - H\left(|x| + \frac{g}{2} - a_1\right). \tag{13}$$

The term $H(y)b/2$ is introduced in Equation (12) to shift the function $s_w^t(x, y)$ upward (along the positive z direction) by an amount equal to half the tow thickness $b/2$ in the region $-a_1/2 \leq x \leq a_1/2$ and $g/2 \leq y \leq a_1/2$.

Similarly, the bottom surface of the warp tow layer could be completely described within the domain of the binary sub-cell no. 1 with the aid of the function:

$$s_w^b(x, y) = \begin{cases} \frac{b}{2}[H(y) - F_H(y)\{H(-y)\text{sign}(y)p_c(x) - R(\text{sign}(y)x, y)p_t(y) \\ -R(-\text{sign}(y)x, y)p_s(y) + H(y)s_{t2}(x, y)\}] \end{cases} \quad (14)$$

in:

$$-\frac{a_1}{2} \leq x \leq \frac{a_1}{2} \quad \text{and} \quad -\frac{a_1}{2} \leq y \leq \frac{a_1}{2}.$$

The notation devised to represent the surface functions of the tow and matrix layers in the current work could be generalized as $s_k^j(i, x, y)$. The subscript, superscript, and arguments of this notation could be assigned different labels to describe the particular surface function in all the six binary sub-cells developed in this work:

$$k = \begin{cases} w & \text{warp tow} \\ f & \text{fill tow} \\ um & \text{upper matrix layer} \\ mm & \text{middle matrix layer} \\ lm & \text{lower matrix layer} \end{cases} \quad (15)$$

$$j = \begin{cases} t & \text{top surface} \\ b & \text{bottom surface} \end{cases} \quad (16)$$

$$i \rightarrow \text{binary sub-cell number}$$

$$x \rightarrow x\text{-axis of binary sub-cell} \quad (17)$$

$$y \rightarrow y\text{-axis of binary sub-cell.}$$

With the aid of the above notation and Equation (12) and (14), the warp tow layer surface functions for binary sub-cell no. 1 are given by:

$$\begin{aligned} s_w^t(1, x, y) &= s_w^t(x, y) \\ s_w^b(1, x, y) &= s_w^b(x, y). \end{aligned} \quad (18)$$

The fill tow surface functions in binary sub-cell no. 1 are then derived in terms of the warp tow surface functions as:

$$\begin{aligned} s_f^t(1, x, y) &= -s_w^b(1, y, x) \\ s_f^b(1, x, y) &= -s_w^t(1, y, x) \end{aligned} \quad (19)$$

The surface plot of Equation (19) representing the spatial variation of the fill tow layer is presented in Figure 11(e).

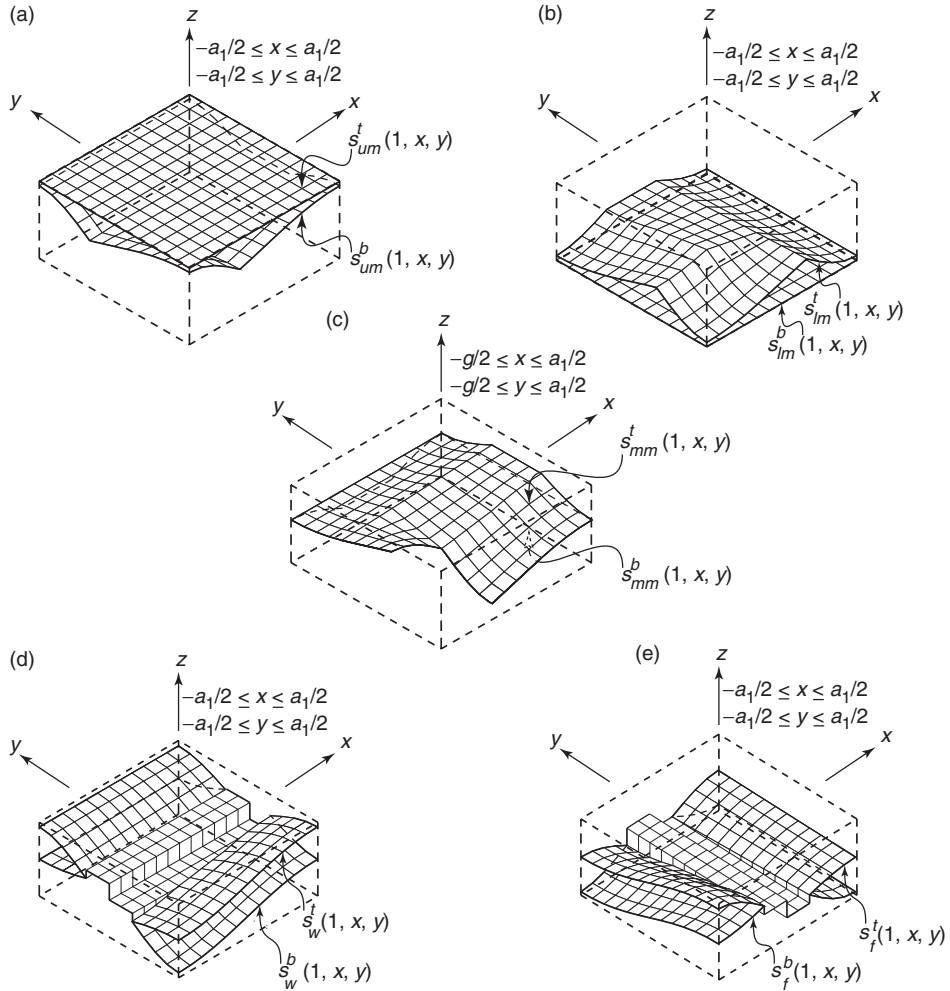


Figure 11. Geometric details of the fiber tow and matrix layer surfaces in binary sub-cell no. 1. (a) Upper matrix layer. (b) Lower matrix layer. (c) Middle matrix layer. (d) Warp tow layer. (e) Fill tow layer.

The fibers within the tows are assumed to be parallel to the centroidal axis of the tows. As such, the angle of rotation of the fibers within the undulating portions of the tows is computed as:

$$\left. \begin{aligned} \theta_y^{uw} &= \operatorname{atan} \left(\frac{\partial (s_w^t(1, x, y))^c}{\partial x} \right) \\ \theta_x^{uf} &= \operatorname{atan} \left(\frac{\partial (s_f^t(1, x, y))^c}{\partial y} \right) \end{aligned} \right\} \quad (20)$$

where the superscript 'c' implies that the derivative is taken with respect to the centroidal path of the fiber tows. Also, in Equation (20) the superscripts uw and uf denote the undulating paths of the warp and fill tows in binary sub-cell no. 1, respectively.

The fibers within the non-undulating paths of the warp and fill tows are aligned along the global X - and Y -directions as shown in Figure 7, respectively. When expanded, the partial derivatives in Equation (20) take the forms:

$$\begin{aligned} \frac{\partial(s_w^t(1, x, y))^c}{\partial x} &= -\frac{\pi b}{2a_1} H(-y) \operatorname{sign}(y) \cos\left(\frac{\pi x}{a_1}\right) \\ \frac{\partial(s_f^t(1, x, y))^c}{\partial y} &= \frac{\pi b}{2a_1} H(-x) \operatorname{sign}(x) \cos\left(\frac{\pi y}{a_1}\right). \end{aligned} \tag{21}$$

Employing the general principles established above, the tow surface functions for the entire library of binary sub-cells developed in this work are reported in Table 3. Note that the surface functions for the binary sub-cell no. 6 are derived in terms of the tow surface functions for the plain weave morphology as discussed in Ref. [1].

Each layer of the matrix material is characterized by a top surface and a bottom surface, as shown in Figure 8. The bottom surface of the upper matrix is defined to be the interface between the top surface of the warp and fill tows and the upper matrix layer that could be derived in terms of the tow surface functions described in Equation (18) and (19). The functional form taken by the bottom surface of the upper matrix is:

$$s_{um}^b(1, x, y) = \begin{cases} \max(s_w^t(1, x, y), s_f^t(1, x, y)) & -\frac{a_1}{2} \leq x \leq \frac{a_1}{2}; \quad -\frac{a_1}{2} \leq y \leq -\frac{g}{2} \\ R^m(y, z_1^1(x, y), z_2^1(x, y)) & -\frac{a_1}{2} \leq x \leq \frac{a_1}{2}; \quad |y| \leq \frac{g}{2} \\ s_w^t(1, x, y) & -\frac{a_1}{2} \leq x \leq \frac{a_1}{2}; \quad \frac{g}{2} \leq y \leq \frac{a_1}{2} \end{cases} \tag{22}$$

where the compound auxiliary function $R^m(x, z_1^1(x, y), z_2^1(x, y))$ linearly interpolates between every point on the two auxiliary functions $z_1^1(x, y)$ and $z_2^1(x, y)$ and is defined as:

$$R^m = z_2^1(x, y) - z_1^1(x, y) \left(\frac{x}{g} + \frac{1}{2}\right) \tag{23}$$

in:

$$|x| \leq \frac{g}{2}.$$

The auxiliary functions $z_1^1(x, y)$ and $z_2^1(x, y)$ are defined as:

$$\left. \begin{aligned} z_1^1(x, y) &= \max(s_w^t(1, x, -g/2), s_f^t(1, x, -g/2)) \\ z_2^1(x, y) &= s_w^t(1, x, g/2). \end{aligned} \right\} \tag{24}$$

The superscript ‘1’ on $z_1^1(x, y)$ and $z_2^1(x, y)$ indicates the binary sub-cell number, which in this case is 1. As the polymer matrix material completely fills the volume exterior to the tows, the top surface of the upper matrix is simply positioned at the overall height of the binary sub-cell. Therefore, the functional form of the top surface of the upper matrix layer is given by:

$$s_{um}^t(1, x, y) = +\frac{h}{2} \tag{25}$$

in:

$$-\frac{a_1}{2} \leq x \leq \frac{a_1}{2}; \quad -\frac{a_1}{2} \leq y \leq \frac{a_1}{2}.$$

With the aid of Equations (22) and (25), the lower matrix top and bottom surfaces could be defined as:

$$\begin{aligned} s_{lm}^t(1, x, y) &= -s_{um}^b(1, y, x) \\ s_{lm}^b(1, x, y) &= -s_{um}^t(1, y, x) = -\frac{h}{2} \end{aligned} \quad (26)$$

in:

$$-\frac{a_1}{2} \leq x \leq \frac{a_1}{2}; \quad -\frac{a_1}{2} \leq y \leq \frac{a_1}{2}.$$

The top and bottom surfaces of the matrix layers derived in Equation (22)–(26) are presented in Figure 11(a) and 11(b), respectively. Due to the orientation of the local coordinate system, only a part of the surface represented by $s_{um}^b(1, x, y)$ is visible in Figure 11(a). However, the top surface of the lower matrix layer $s_{lm}^t(1, x, y)$ being an anti-symmetric reflection of $s_{um}^b(1, x, y)$, clearly displays the complex nature of this matrix layer surface.

The middle matrix layer too is mathematically described by top and bottom surfaces, the expressions for which are derived in terms of the top surface functions and the appropriate auxiliary functions in a manner similar to that used in mathematically describing the upper and lower matrix layers. As such, the top surface of the middle matrix layer is given by:

$$s_{mm}^t(1, x, y) = \begin{cases} s_w^b(1, x, y) & -\frac{g}{2} \leq x \leq \frac{a_1}{2}; \quad -\frac{g}{2} \leq y \leq \frac{a_1}{2} \\ R^m(y, z_1^1(x, y), z_2^1(x, y)) & -\frac{a_1}{2} \leq x \leq \frac{a_1}{2}; \quad |y| \leq \frac{g}{2} \\ s_w^b(1, x, y) & -\frac{a_1}{2} \leq x \leq \frac{a_1}{2}; \quad \frac{g}{2} \leq y \leq \frac{a_1}{2} \end{cases} \quad (27)$$

where the compound auxiliary function $R^m(y, z_1^1(x, y), z_2^1(x, y))$ is defined in Equation (23) and the auxiliary functions $z_1^1(x, y)$ and $z_2^1(x, y)$ are given by:

$$\left. \begin{aligned} z_1^1(x, y) &= \max\left(s_w^t(1, x, -g/2), s_f^t(1, x, -g/2)\right) \\ z_2^1(x, y) &= s_w^b(1, x, g/2). \end{aligned} \right\} \quad (28)$$

The bottom surface of the middle matrix is an anti-symmetric reflection of the top surface. Therefore, the functional form of the bottom surface of the middle matrix is written as:

$$s_{mm}^b(1, x, y) = -s_{mm}^t(1, y, x)$$

where:

$$-\frac{a_1}{2} \leq x \leq \frac{a_1}{2}; \quad -\frac{a_1}{2} \leq y \leq \frac{a_1}{2} \quad (29)$$

The surface plot of the middle matrix layer comprising the top and bottom surfaces is presented in Figure 11(c). Note that the middle matrix layer is not defined in the interlace region characterized by $x \leq -g/2$ and $y \leq -g/2$. Everywhere else in the binary sub-cell no. 1 the top and bottom surfaces of the middle matrix layer are defined as appropriate interface

functions between the tow layers. For the sake of completeness we have presented the warp and fill tow layers in binary sub-cell no. 1 in Figure 11(d) and (e), respectively.

The matrix layer surface functions in binary sub-cells nos. 2 through 6 could be derived in terms of the respective tow surface functions in a manner similar to that used in sub-cell no. 1. Taking advantage of the similarities between various binary sub-cells as explained earlier, the matrix layer surface functions in binary sub-cells nos. 2 through 6 are reported in a tabular format as shown in Table 4 and 5. Here once again we note that the matrix layer surface functions in binary sub-cell no. 6 are derived in terms of the plain weave morphology matrix layer surface functions, as discussed in Ref. [1].

Layered Matrix Model for the Binary Sub-cell no. 1

Woven fabric ceramic matrix composites (CMCs) fabricated via the chemical vapor infiltration (CVI) technique are most often characterized by large macroscopic voids [1,3,19–21]. As a result, the matrix material in CVI woven CMCs appears as a non-uniform layer of spatially varying thickness.

Consistent with the modeling approach of Kuhn and Charalambides [1], schematic representation of a three ply 5HS CVI SiC laminate is shown in Figure 12(a). In this figure, the darkened regions represent the large scale inter-connected network of matrix voids, whereas the matrix material itself is shown as a layer over the tows. The full representative unit-cell of the 5HS woven system is shown isolated within the rectangle in Figure 12(a). In Figure 12(b), the full unit-cell is extracted from the laminate of Figure 12(a) and the bounds of the basic or repeating unit-cell (RUC) are established. The RUC is then extracted from within the full unit-cell as shown in Figure 12(c), where an

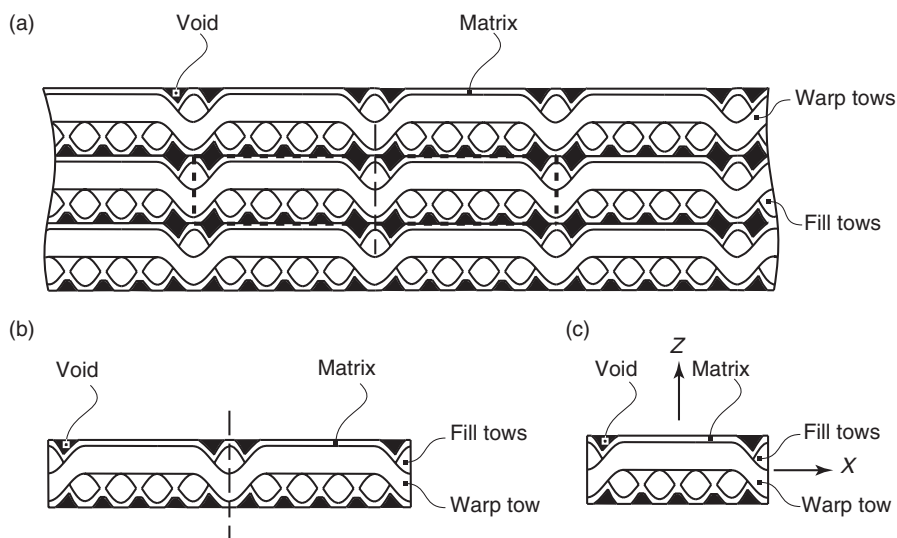


Figure 12. Schematic representation of the cross-section of a five harness woven laminate. (a) Identification of the representative unit cell in the layered matrix model. (b) Detailed view of the representative unit cell showing the fiber tows and matrix material. (c) The schematic representation of the basic or repeating unit cell (RUC) in the layered matrix model. Mathematical surface functions are developed to describe the fiber tow and matrix layer topology within the RUC.

appropriate coordinate system with the positive Z -axis pointing upward is established. The matrix layer in Figure 12(c) appears as a non-uniform layer of spatially varying thickness and is truncated at the overall height of the repeating unit-cell as it is extracted from the laminate configuration of Figure 12(c). As such, an additional geometry parameter t representing the thickness of the matrix material is introduced in the modeling, as shown schematically in Figure 13. The other geometry parameters shown in Figure 13 retain the same meaning as described in the porous matrix model presented in the previous sub-section.

A representative 3D finite element mesh of binary sub-cell no. 1 with a non-uniform layer of inter-tow matrix characterized by a central hole in the gap region between the tows is presented in Figure 14. In real material systems, these holes may exhibit a rather non-uniform 3D shape which may be approximated using circular, square or elliptical cross-sections. However, in this work, the inter-connected matrix voids are modeled as a funnel ending with a cylindrical stem in the tow region as shown in the isometric views of Figure 14(a) and (b). The sectioned gap region views displayed in Figure 15(b) and (c) illustrate the shape of the matrix material external to the tows. The spatially varying thickness of the middle matrix layer is equal to the magnitude of the difference between the top and bottom surfaces. The volume between the top and bottom surfaces of the middle matrix layer is assumed to be completely filled with matrix material and as such is not characterized by a unique geometry parameter.

Fiber tow architecture in the present layered matrix model are also described by Equations (18) and (19). The upper and lower matrix layers $s_{um}^t(1, x, y)$ and $s_{lm}^b(1, x, y)$ respectively, are taken to be non-uniform characterized by the spatially varying thickness $t_m(x, y)$ and incorporating a circular hole. The middle matrix layer although completely filled is modeled with a circular hole to fully define the cylindrical matrix void in the center

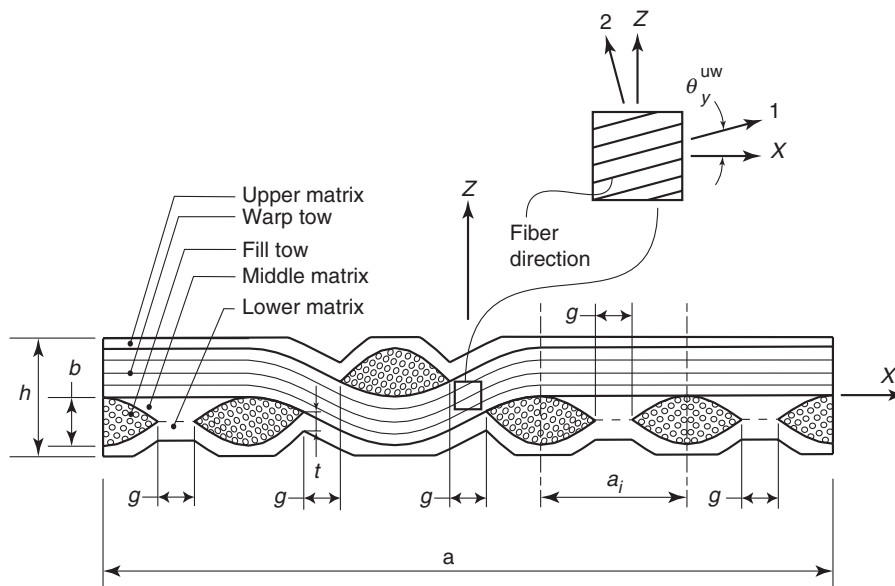


Figure 13. Geometry parameters employed in the 5HS layered matrix model. Note that the upper and lower matrix layers are truncated at the overall height of the unit-cell with their thickness monitored by the parameter t . On the other hand, the middle matrix layer above the dashed lines is assumed to be completely filled.

of the binary sub-cell no. 1. The functional form of the spatially varying matrix thickness is written as follows:

$$t_m(x, y) = \begin{cases} 0 & f(x, y) < \frac{g}{2} - t \\ \frac{1}{2}f(x, y) + t - \frac{g}{4} & \frac{g}{2} - t \leq f(x, y) < \frac{g}{2} \\ t & \frac{g}{2} \leq f(x, y) \end{cases} \quad (30)$$

where the spatial function $f(x, y)$ could represent a circle, ellipse or square:

$$f(x, y) = \begin{cases} \sqrt{x^2 + y^2} & \text{circle} \\ \sqrt{(x/c)^2 + (y/e)^2} & \text{ellipse} \\ \max(|x|, |y|) & \text{square.} \end{cases} \quad (31)$$

In Equation (31), $2c$ and $2e$ represent the major and minor axes of the ellipse.

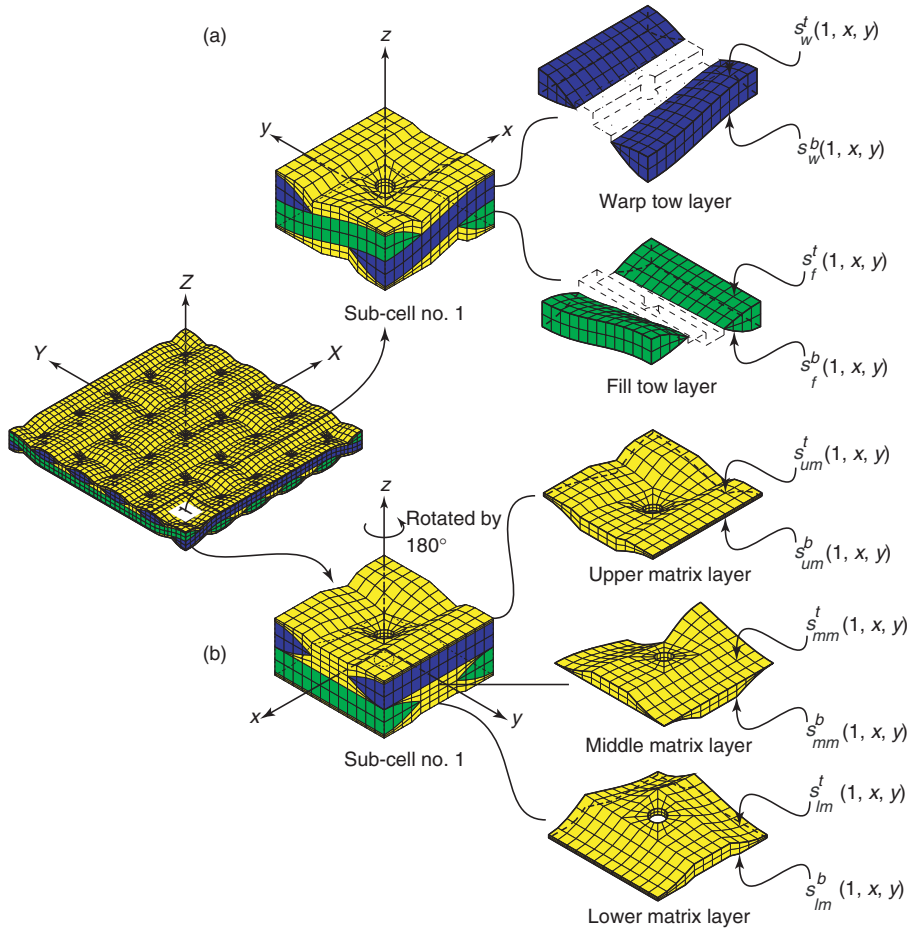


Figure 14. Geometric details of the binary sub-cell no. 1 showing blow-up isometric views of individual layers incorporating a central hole representative of the macroscopic porosity in CVI CMCs.

Incorporating the spatial definition of the matrix layer thickness given in Equation (30), the surface functions for the top and bottom surfaces of the upper and lower matrix layers could be written in terms of the tow/matrix interface functions $s_{um}^b(1, x, y)$ and $s_{lm}^t(1, x, y)$ given by Equations (22) and 26, respectively:

$$s_{um}^t(1, x, y) = \min\left(s_{um}^b(1, x, y) + t_m(x, y), +\frac{h}{2}\right) \quad (\text{upper matrix}) \quad (32)$$

and:

$$s_{lm}^b(1, x, y) = \max\left(s_{lm}^t(1, x, y) - t_m(x, y), -\frac{h}{2}\right) \quad (\text{lower matrix}) \quad (33)$$

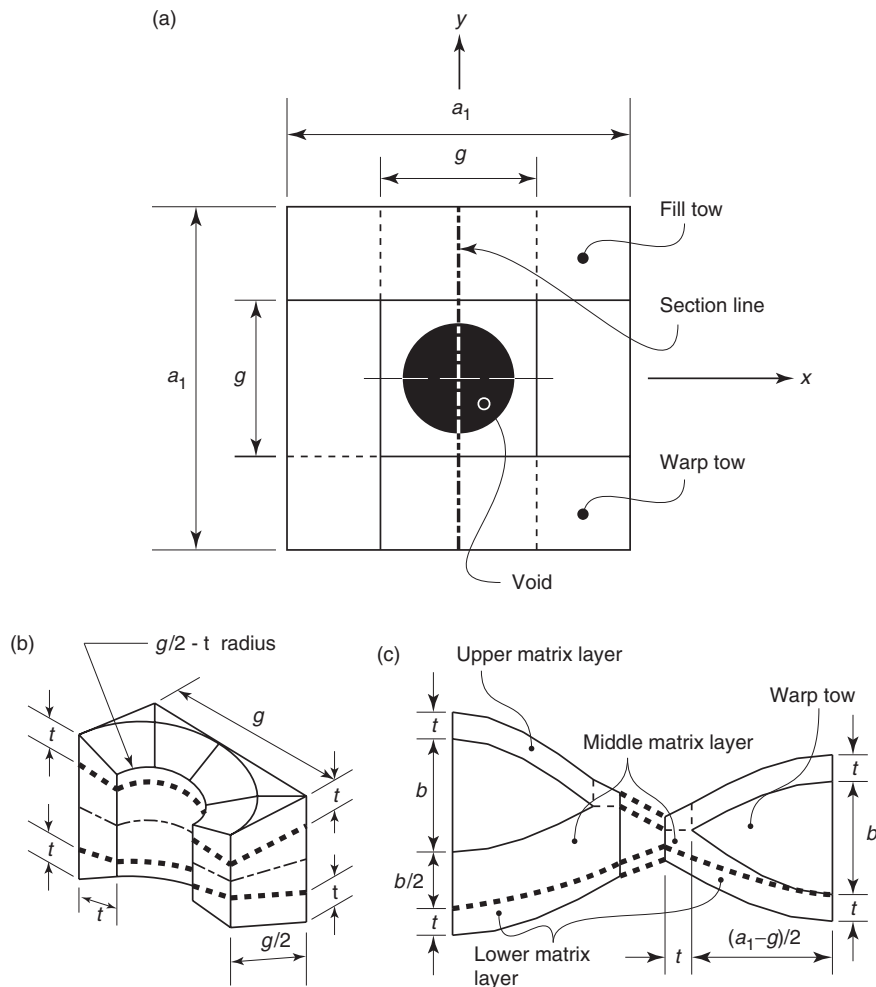


Figure 15. Geometric details of the matrix layer in binary sub-cell no. 1 near the vicinity of the central cylindrical void. (a) Top view of binary sub-cell no. 1 showing the imprint of the tow architecture. (b) Matrix material in the gap region. (c) Matrix material surrounding the tows in the bridging region. Note the clear distinction between the upper matrix, middle matrix and lower matrix layers.

Equation (32) and (33) represent the top surface of the upper matrix and bottom surface of the lower matrix respectively. The expressions for the bottom surface of the upper matrix $s_{um}^b(1, x, y)$ and top surface of the lower matrix $s_{lm}^t(1, x, y)$ are given by Equations (22) and (26), respectively. The top and bottom surfaces of the middle matrix layer $s_{mm}^t(1, x, y)$ and $s_{mm}^b(1, x, y)$ remain the same as those in Equations (27) and (29), respectively. Each of the matrix layer surfaces as described by Equations (22), (26), (27), (29), (32), and (33) are presented in Figure 16.

The expressions for the top surface of the upper matrix and bottom surface of the lower matrix for the binary sub-cells nos. 2 through 6 in terms of the respective tow/matrix interface surface functions could be tabulated as shown in Table 6. The other matrix layer surface functions in these binary sub-cells remain unaltered.

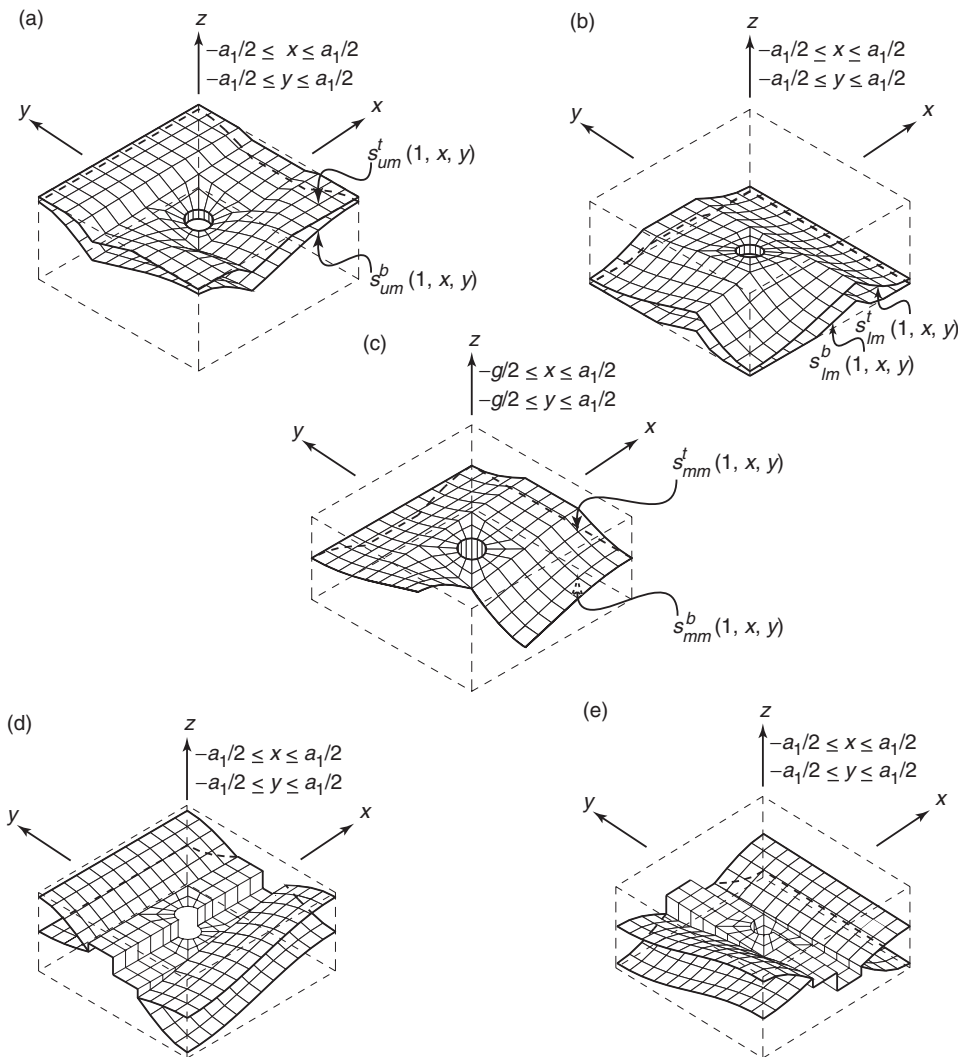


Figure 16. Geometric details of the fiber tow and matrix layer surfaces in binary sub-cell no. 1. (a) Upper matrix layer. (b) Lower matrix layer. (c) Middle matrix layer. (d) Warp tow layer. (e) Fill tow layer.

ASSEMBLING THE REPEATING UNIT-CELLS OF SATIN WEAVE FABRIC COMPOSITES

The global position of an individual binary sub-cell within the unit-cell domain (see Figures 4(a), 5(a) and (b)) is determined by defining a square global position matrix (GPM), with dimensions of $N_g \times N_g$, where N_g is the minimum loom harness number. The elements of $\text{GPM}(N_g, N_g)$, store the address of the individual binary sub-cell within the unit-cell domain of each satin weave fabric. In particular, for the 4HS satin weave, the dimensions of $\text{GPM}(N_g, N_g)$ are $\text{GPM}(4, 4)$, with the 5HS and 8HS satin weaves associated with a GPM matrix of dimensions $\text{GPM}(5, 5)$ and $\text{GPM}(8, 8)$, respectively. In addition to $\text{GPM}(N_g, N_g)$, we need to define two global position vectors $\text{GCX}(N_g)$ and $\text{GCY}(N_g)$, the elements of which contain the global X and Y centroidal coordinates of each binary sub-cell relative to the global XYZ directions of the individual basic or repeating unit-cells as shown in Figure 4.

The unit-cells of the satin weave fabrics are modeled with spatial dimensions $a \times a \times h$. The parameter a represents the in-plane dimensions of the unit-cells, while h is the overall height of one ply of the satin weave fabric composite. In real systems, the magnitude of a could be of the order of 6–12 mm [3,21] in satin weave ceramic matrix composites (CMCs), while in the case of PW CMCs, a could be of the order of 1–2 mm. Consistent with the discussions in Refs [1,22,23], a general non-dimensional modeling environment lends easily to performing broad parametric studies aimed at investigating the effect of various micro-constituent parameters on the macroscopic response of satin weave fabric composites. When conducting non-dimensional simulations, it is often convenient to normalize the woven unit-cell geometry with respect to the above mentioned parameter a . In such a case, the parameter a is chosen as the characteristic in-plane dimension resulting in:

$$\hat{a} = a/a = 1 \quad (34)$$

where ($\hat{\quad}$) denotes a non-dimensional quantity. Since N_g number of unique binary sub-cells are required to assemble the complete unit-cells of the corresponding satin weave fabrics, the in-plane dimensions of each binary sub-cell are computed as:

$$a_i = a/N_g \quad i \rightarrow \text{binary sub-cell number.} \quad (35)$$

Employing the above normalization, we have:

$$\hat{a}_i = a_i/a \quad i \rightarrow \text{binary sub-cell number.} \quad (36)$$

Therefore it is evident from Equations (35) and (36) that:

$$\hat{a}_i = \begin{cases} 1/4 & \text{4HS satin weave} \\ 1/5 & \text{5HS satin weave} \\ 1/8 & \text{8HS satin weave.} \end{cases} \quad (37)$$

Similarly, the other geometry parameters introduced to model repeating unit-cells of the satin weave fabric composites are normalized as:

$$\begin{aligned}\hat{b} &= b/a \\ \hat{g} &= g/a \\ \hat{h} &= h/a \\ \hat{t} &= t/a\end{aligned}\quad (38)$$

As a result of the above normalization procedure, each binary sub-cell occupies the non-dimensional volume of $\hat{a}_i \times \hat{a}_i \times \hat{h}$. With the aid of Equation (37) and the knowledge that N_g binary sub-cells constitute the longitudinal and transverse directions of the repeating unit-cells of the particular woven system, it becomes evident that upon the assemblage of N_g unique binary sub-cells the overall geometric dimensions of the complete repeating unit-cell would be $1 \times 1 \times \hat{h}$. In the above expressions, $\hat{h} = h/a$ is the normalized height of the woven ply. The minimum admissible height of the woven unit-cell is given by $\hat{h} = 2\hat{b}$, where $\hat{b} = b/a$ is the normalized maximum tow thickness.

Since the mathematical surface functions are defined relative to the local xyz coordinate systems of the individual binary sub-cells, it becomes useful to derive general relations between the local and global normalized quantities. As such, we define normalized geometry parameters relative to the individual binary sub-cells:

$$\begin{aligned}\hat{b}_i &= b/a_i \\ \hat{g}_i &= g/a_i \\ \hat{h}_i &= h/a_i \\ \hat{t}_i &= t/a_i.\end{aligned}\quad (39)$$

Substituting $a_i = a\hat{a}_i$ from Equation (36) into Equation (39), we get:

$$\begin{aligned}b &= \hat{a}_i\hat{b}_i a \\ g &= \hat{a}_i\hat{g}_i a \\ h &= \hat{a}_i\hat{h}_i a \\ t &= \hat{a}_i\hat{t}_i a\end{aligned}\quad (40)$$

and hence the relations between the local and global normalized geometry parameters are given by:

$$\begin{aligned}\hat{b} &= b/a = \hat{a}_i\hat{b}_i \\ \hat{g} &= g/a = \hat{a}_i\hat{g}_i \\ \hat{h} &= h/a = \hat{a}_i\hat{h}_i \\ \hat{t} &= t/a = \hat{a}_i\hat{t}_i.\end{aligned}\quad (41)$$

With the aid of the above information, we can now build $GPM(N_g, N_g)$, ensuring the global origin of the repeating unit-cell to be located at the geometric center. The global location of each binary sub-cell in the 4HS, 5HS, and 8HS woven systems are reported in Table 1. The elements of the global position vectors $GcX(N_g)$ and $GcY(N_g)$ storing the centroidal coordinates of each binary sub-cell in the 4HS, 5HS and 8HS woven systems are reported in Table 2.

Table 1. Binary sub-cell positioning matrix for satin weave composites.

(a) Four Harness Satin Weave Global Position Matrix								
Sub-cell no.	Location in positioning matrix							
1	GPM(1,3)	GPM(2,2)	GPM(3,1)	GPM(4,4)				
4	GPM(1,1)	GPM(2,4)	GPM(3,3)	GPM(4,2)				
5	GPM(1,2)	GPM(2,1)	GPM(3,4)	GPM(4,3)				
6	GPM(1,4)	GPM(2,3)	GPM(3,2)	GPM(4,1)				

(b) Five Harness Satin Weave Global Position Matrix					
Sub-cell no.	Location in positioning matrix				
1	GPM(1,3)	GPM(2,1)	GPM(3,4)	GPM(4,2)	GPM(5,5)
2	GPM(1,5)	GPM(2,3)	GPM(3,1)	GPM(4,4)	GPM(5,2)
3	GPM(1,4)	GPM(2,2)	GPM(3,5)	GPM(4,3)	GPM(5,1)
4	GPM(1,1)	GPM(2,4)	GPM(3,2)	GPM(4,5)	GPM(5,3)
5	GPM(1,2)	GPM(2,5)	GPM(3,3)	GPM(4,1)	GPM(5,4)

(c) Eight Harness Satin Weave Global Position Matrix								
Sub-cell no.	Location in positioning matrix							
1	GPM(1,3)	GPM(2,6)	GPM(3,1)	GPM(4,4)	GPM(5,7)	GPM(6,2)	GPM(7,5)	GPM(8,8)
2	GPM(1,4)	GPM(2,7)	GPM(3,2)	GPM(4,5)	GPM(5,8)	GPM(6,3)	GPM(7,6)	GPM(8,1)
3	GPM(1,8)	GPM(2,3)	GPM(3,6)	GPM(4,1)	GPM(5,4)	GPM(6,7)	GPM(7,2)	GPM(8,5)
4	GPM(1,1)	GPM(2,4)	GPM(3,7)	GPM(4,2)	GPM(5,5)	GPM(6,8)	GPM(7,3)	GPM(8,6)
5	GPM(1,2)	GPM(2,1)	GPM(3,3)	GPM(4,3)	GPM(5,1)	GPM(6,1)	GPM(7,1)	GPM(8,2)
5	GPM(1,5)	GPM(2,2)	GPM(3,4)	GPM(4,6)	GPM(5,2)	GPM(6,4)	GPM(7,4)	GPM(8,3)
5	GPM(1,6)	GPM(2,5)	GPM(3,5)	GPM(4,7)	GPM(5,3)	GPM(6,5)	GPM(7,7)	GPM(8,4)
5	GPM(1,7)	GPM(2,8)	GPM(3,8)	GPM(4,8)	GPM(5,6)	GPM(6,6)	GPM(7,8)	GPM(8,7)

Table 2. The global positioning vectors for satin weave composites.

(a) Four Harness Satin Weave Centroidal Position Vectors				
Vector	Element			
$\overline{GCX} =$	$\{1.5a_i$	$0.5a_i$	$-0.5a_i$	$-1.5a_i\}$
$\overline{GCY} =$	$\{1.5a_i$	$0.5a_i$	$-0.5a_i$	$-1.5a_i\}$

(b) Five Harness Satin Weave Centroidal Position Vectors				
Vector	Element			
$\overline{GCX} =$	$\{2a_i$	a_i	0.0	$-a_i - 2a_i\}$
$\overline{GCY} =$	$\{2a_i$	a_i	0.0	$-a_i - 2a_i\}$

(c) Eight Harness Satin Weave Centroidal Position Vectors								
Vector	Element							
$\overline{GCX} =$	$\{3.5a_i$	$2.5a_i$	$1.5a_i$	$0.5a_i$	$-0.5a_i$	$-1.5a_i$	$-2.5a_i$	$-3.5a_i\}$
$\overline{GCY} =$	$\{3.5a_i$	$2.5a_i$	$1.5a_i$	$0.5a_i$	$-0.5a_i$	$-1.5a_i$	$-2.5a_i$	$-3.5a_i\}$

FINITE ELEMENT DISCRETIZATION OF SATIN WEAVE FABRICS

The tow surface functions for the binary sub-cell no. 1 in Equations (18) and (19) may be utilized to generate and locate nodes on the surface of the tows. The nodes in the interior of the tows may then be interpolated from these surface nodes and the resulting array

Table 3. Surface functions derived for the warp and fill tows in binary sub-cells nos. 2 through 6. The tow surface functions for binary sub-cell no. 6 are derived in terms of the warp and fill tow layer functions for the plain weave system presented in Ref. [1].

(a) Warp Tow Surface Functions		
Sub-cell no.	Top surface	Bottom surface
2	$s_w^t(2, x, y) = s_w^t(1, -x, y)$	$s_w^b(2, x, y) = s_w^b(1, -x, y)$
3	$s_w^t(3, x, y) = s_w^t(1, x, -y)$	$s_w^b(3, x, y) = s_w^b(1, x, -y)$
4	$s_w^t(4, x, y) = s_w^t(1, -x, -y)$	$s_w^b(4, x, y) = s_w^b(1, -x, -y)$
5	$s_w^t(5, x, y) = -\frac{b}{2} F_H(y) \text{sign}(-y) \rho_s(y)$	$s_w^b(5, x, y) = -s_w^t(5, x, y) + b$
6	$s_w^t(6, x, y) = s_w^t(-x, y)$	$s_w^b(6, x, y) = s_w^b(-x, y)$

(b) Fill Tow Surface Functions		
Sub-cell no.	Top surface	Bottom surface
2	$s_f^t(2, x, y) = s_f^t(1, -x, y)$	$s_f^b(2, x, y) = s_f^b(1, -x, y)$
3	$s_f^t(3, x, y) = s_f^t(1, x, -y)$	$s_f^b(3, x, y) = s_f^b(1, x, -y)$
4	$s_f^t(4, x, y) = s_f^t(1, -x, -y)$	$s_f^b(4, x, y) = s_f^b(1, -x, -y)$
5	$s_f^t(5, x, y) = s_w^t(5, y, x) - b$	$s_f^b(5, x, y) = s_w^b(5, y, x) - b$
6	$s_f^t(6, x, y) = -s_w^b(-y, x)$	$s_f^b(6, x, y) = s_w^t(-y, x)$

of nodes may be used to form 3D eight- or twenty-node isoparametric elements. The mesh of the tows so generated may then be translated to the appropriate positions occupied by the binary sub-cell no. 1 within the unit-cells of different satin weave fabrics with the aid of the information provided in Table 1 and 2. This procedure is repeated for each binary sub-cell assembled to formulate the numerical 3D finite element models of the 4HS, 5HS, and 8HS woven fabrics studied in this work. However, care should be taken to ensure that the nodes on the interfaces of the tow and matrix layers are aligned and that coincident nodes should either be constrained as needed to preserve displacement continuity or duplicate nodes should be removed.

Satin weave fabric matrix material finite element meshes may be generated in a similar manner by employing Equations (22)–(29) in the binary sub-cell no. 1 and corresponding equations in binary sub-cells nos. 2 through 6 from Table 4 and 5 for the porous matrix model. While modeling the layered matrix over the tows and incorporating macroscopic porosity, the matrix layer surface functions given by Equations (32) and (33) for the top and bottom surfaces of the upper and lower matrix layers in binary sub-cell no. 1 need to be employed. Similar expressions for the top and bottom surfaces of the upper and lower matrix layers in binary sub-cells nos. 2 through 6 must be used from Table 6.

The 4HS, 5HS, and 8HS satin weave fiber tow 3D finite element meshes shown in Figure 17(a) were generated using the principle explained above. In these figures, numbers enclosed in boxes refer to different locations of each binary sub-cell used to generate the complete unit-cells. In particular, the finite element mesh of the fiber tows in the 4HS woven fabric shown in Figure 17(a) was generated using 3072 3D eight-node isoparametric elements with a total of 8448 nodes. Similarly, the tows in the 5HS woven fabric were meshed using 4800 3D eight-node isoparametric elements with a total of 13,200 nodes, while the fiber tows in the 8HS woven system were discretized using 12,288 3D eight-node isoparametric elements with a total of 33,792 nodes.

Table 4. Surface functions derived for the upper and lower matrix layers in binary sub-cells nos. 2 through 6. The bottom surface function of the upper matrix layer in binary sub-cell no. 6 is derived in terms of the warp and fill tow layer functions for the plain weave system presented in Ref. [1]. The superscript 5 on $z_1^5(x, y)$ and $z_2^5(x, y)$ indicates the binary sub-cell no. 5. The bottom surface of the upper matrix layer in binary sub-cell no. 5 is described using Equation (22) with $z_1^5(x, y)$ and $z_2^5(x, y)$ substituted for $z_1^1(x, y)$ and $z_2^1(x, y)$, respectively.

(a) Auxiliary Functions For Binary Sub-Cell No. 5		
Sub-cell no.	Auxiliary function $z_1^5(x, y)$	Auxiliary function $z_2^5(x, y)$
5	$\max((s_w^t(5, x, -g/2), s_f^t(5, x, -g/2)))$	$s_w^t(5, x, g/2)$

(b) Upper Matrix Layer Surface Functions		
Sub-cell no.	Bottom surface	Top surface
2	$s_{um}^b(2, x, y) = s_{um}^b(1, -x, y)$	$s_{um}^t(2, x, y) = +\frac{h}{2}$
3	$s_{um}^b(3, x, y) = s_{um}^b(1, x, -y)$	$s_{um}^t(3, x, y) = +\frac{h}{2}$
4	$s_{um}^b(4, x, y) = s_{um}^b(1, -x, -y)$	$s_{um}^t(4, x, y) = +\frac{h}{2}$
5	$s_{um}^b(5, x, y) = s_{um}^b(1, x, y)$	$s_{um}^t(5, x, y) = +\frac{h}{2}$
6	$s_{um}^b(6, x, y) = \max(s_w^t(6, x, y), s_f^t(6, x, y))$	$s_{um}^t(6, x, y) = +\frac{h}{2}$

(c) Lower Matrix Layer Surface Functions		
Sub-cell no.	Top surface	Bottom surface
2	$s_{lm}^t(2, x, y) = -s_{um}^b(2, -y, -x)$	$s_{lm}^b(2, x, y) = -\frac{h}{2}$
3	$s_{lm}^t(3, x, y) = -s_{um}^b(3, -y, -x)$	$s_{lm}^b(3, x, y) = -\frac{h}{2}$
4	$s_{lm}^t(4, x, y) = -s_{um}^b(4, y, x)$	$s_{lm}^b(4, x, y) = -\frac{h}{2}$
5	$s_{lm}^t(5, x, y) = -s_{um}^b(5, y, x)$	$s_{lm}^b(5, x, y) = -\frac{h}{2}$
6	$s_{lm}^t(6, x, y) = -s_{um}^b(6, y, x)$	$s_{lm}^b(6, x, y) = -\frac{h}{2}$

Table 5. Surface functions derived for the middle matrix layers in binary sub-cells nos. 2 through 5. The superscript 5 on $z_1^5(x, y)$ and $z_2^5(x, y)$ indicates the binary sub-cell no. 5. The top surface of the middle matrix layer in binary sub-cell no. 5 is described using Equation (27) with $z_1^5(x, y)$ and $z_2^5(x, y)$ substituted for $z_1^1(x, y)$ and $z_2^1(x, y)$, respectively.

(a) Auxiliary Functions For Binary Sub-Cell No. 5		
Sub-cell no.	Auxiliary Function $z_1^5(x, y)$	Auxiliary Function $z_2^5(x, y)$
5	$\max((s_w^t(5, x, -g/2), s_f^t(x, -g/2)))$	$s_w^b(x, g/2)$

(b) Middle Matrix Layer Surface Functions		
Sub-cell no.	Top surface	Bottom surface
2	$s_{mm}^t(2, x, y) = s_{mm}^t(1, -x, y)$	$s_{mm}^b(2, x, y) = -s_{mm}^b(2, y, x)$
3	$s_{mm}^t(3, x, y) = s_{mm}^t(1, x, -y)$	$s_{mm}^b(3, x, y) = -s_{mm}^b(3, y, x)$
4	$s_{mm}^t(4, x, y) = s_{mm}^t(1, -x, -y)$	$s_{mm}^b(4, x, y) = -s_{mm}^b(4, y, x)$
5	$s_{mm}^t(5, x, y) = s_{mm}^t(1, x, y)$	$s_{mm}^b(5, x, y) = -s_{mm}^b(5, y, x)$

Table 6. Surface functions derived for the top and bottom surfaces of the upper and lower matrix layers in binary sub-cells nos. 2 through 6 associated with the layered matrix model. Note that the bottom and top surface functions of the upper and lower matrix layers in binary sub-cell nos. 2 through 6 remain unchanged and are as such given in Table 4.

(a) Upper Matrix Layer Top Surface Functions	
Sub-cell no.	Top surface
2	$s_{um}^t(2, x, y) = \min(s_{um}^b(2, x, y) + t_m(x, y), + \frac{h}{2})$
3	$s_{um}^t(3, x, y) = \min(s_{um}^b(3, x, y) + t_m(x, y), + \frac{h}{2})$
4	$s_{um}^t(4, x, y) = \min(s_{um}^b(4, x, y) + t_m(x, y), + \frac{h}{2})$
5	$s_{um}^t(5, x, y) = \min(s_{um}^b(5, x, y) + t_m(x, y), + \frac{h}{2})$
6	$s_{um}^t(6, x, y) = \min(s_{um}^b(6, x, y) + t_m(x, y), + \frac{h}{2})$

(b) Lower Matrix Layer Bottom Surface Functions	
Sub-cell no.	Bottom surface
2	$s_{lm}^b(2, x, y) = \max(s_{lm}^t(2, x, y) - t_m(x, y), - \frac{h}{2})$
3	$s_{lm}^b(3, x, y) = \max(s_{lm}^t(3, x, y) - t_m(x, y), - \frac{h}{2})$
4	$s_{lm}^b(4, x, y) = \max(s_{lm}^t(4, x, y) - t_m(x, y), - \frac{h}{2})$
5	$s_{lm}^b(5, x, y) = \max(s_{lm}^t(5, x, y) - t_m(x, y), - \frac{h}{2})$
6	$s_{lm}^b(6, x, y) = \max(s_{lm}^t(6, x, y) - t_m(x, y), - \frac{h}{2})$

The complete 3D finite element meshes of the 4HS, 5HS, and 8HS woven systems incorporating a porous polymer matrix material are presented in Figure 17(b). In this case, the 4HS woven fabric unit-cell was discretized with 5816 3D eight-node isoparametric elements using a total of 18,840 nodes. Similarly, the 5HS woven morphology was made with 9420 3D eight-node isoparametric elements employing a total of 30,710 nodes, while the 8HS woven fabric unit-cell was discretized with 24,288 3D eight-node isoparametric elements with a total of 79,232 nodes.

A layered ceramic matrix material exhibiting macroscopic porosity was modeled over the tows in 4HS, 5HS, and 8HS woven fabrics incorporating large-scale matrix voids as shown in Figure 17(c). The unit-cell of the 4HS woven system in this case was modeled with 6344 3D eight-node isoparametric elements with a total of 24,448 nodes. The 5HS satin weave fabric repeating unit-cell was discretized with 10320 3D eight-node isoparametric elements employing a total of 40,160 nodes. However, owing to a different fiber architecture characterized by greater volume fraction of straight and non-undulating fiber tows, the unit-cell of the 8HS woven fabric with a ceramic–matrix material deposited over the fiber tows was modeled with 26,592 3D eight-node isoparametric elements using a total of 103,424 nodes.

The finite element meshes shown in Figure 17 are presented to illustrate the outcome of the meshing methodology while the mesh size numbers discussed above provide a sense of the size of the problem. The density of actual finite element meshes employed to solve particular boundary value problems reported in Ref. [12] were selected through broad mesh sensitivity studies. While the meshes shown in Figure 17 were discretized with eight-noded brick elements, the ability to incorporate twenty-noded brick elements is inherently built into the programming routines. The choice of the particular element depends on available computing resources.

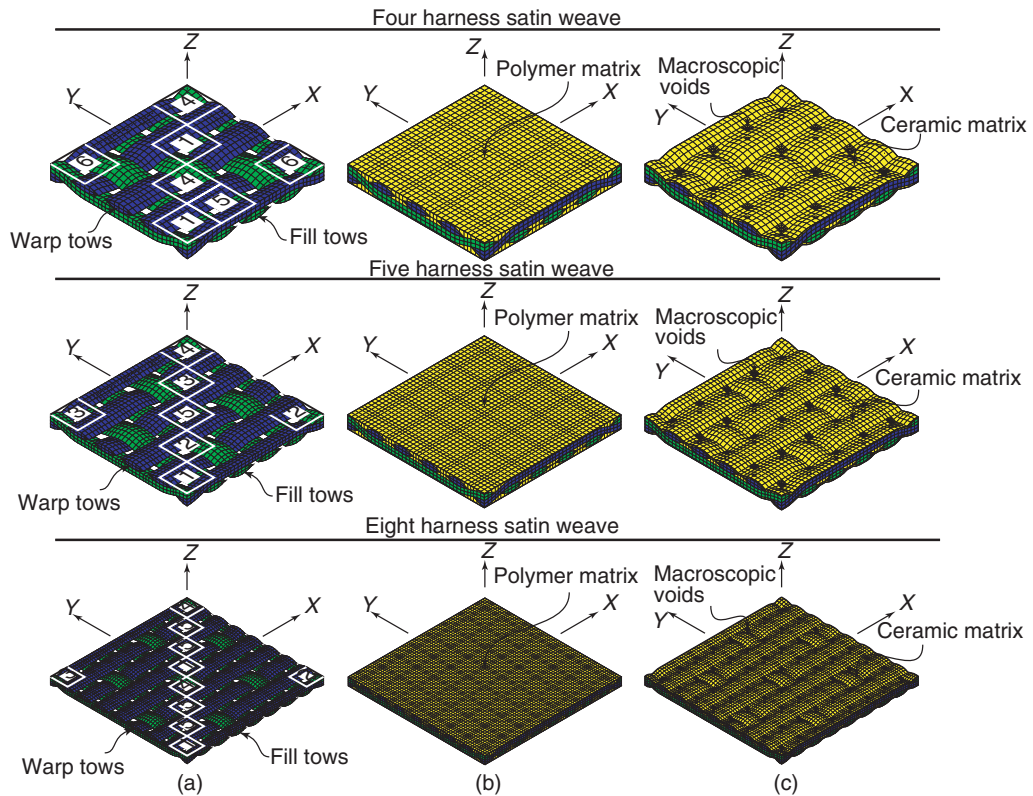


Figure 17. Finite element meshes of the repeating unit-cells of satin weave fabric composites constructed with geometry parameters $b/a_i = 0.2$, $g/a_i = 0.2$ and $h/a_i = 0.45$. The parameter a_i for the individual weave architectures is computed with the aid of Equation (35). Column (a) The fiber tow architecture within the domain of the repeating unit-cells of individual weaves. Column (b) Repeating unit-cells of the 4HS, 5HS and 8HS woven fabrics impregnated with a porous polymer matrix. Column (c) Repeating unit-cells of the 4HS, 5HS and 8HS woven fabrics impregnated with a layered ceramic matrix. In this case, the normalized thickness of the matrix material is given by $t/a_i = 0.05$, where a_i is again computed with the aid of Equation (35) for individual weaves. All meshes were constructed using 3D eight-node isoparametric elements.

MICRO-CONSTITUENT VOLUME FRACTIONS

The mathematical surface functions developed in previous sections are now employed to calculate the fiber bundle and matrix volume fractions in the 4HS, 5HS, and 8HS satin weave PMCs and CMCs. The volume fraction of the warp tows is given by $v_{\text{warp}} = V_{\text{warp}}/V_{\text{total}}$, where the lower case v denotes the volume fraction of the quantity indicated by the subscript, while the V denotes the volume occupied by the same micro-constituent. V_{total} represents the total volume of the complete unit-cell which is given by $V_{\text{total}} = ha^2$, where h is the overall height of the woven ply. Since the minimum admissible height of the woven ply is $h = 2b$, the total volume of the unit-cell could also be written as $V_{\text{total}} = 2ba^2$. The volume V_{warp} occupied by the warp bundles within the unit-cell can be calculated by summing up the volume occupied by the warp bundles in the individual binary sub-cells in the complete unit-cell of each woven system.

Accordingly, the volume occupied by the warp bundles in the unit-cell of individual satin weave fabrics is given by:

$$V_{\text{warp}} = \sum_{m=1}^{N_g} \sum_{n=1}^{N_g} \left[\int_{-a_i/2}^{a_i/2} \int_{-a_i/2}^{a_i/2} \{s_w^t(i, x, y) - s_w^b(i, x, y)\} dy dx \right] \quad (42)$$

where $i = \text{GPM}[m, n]$ represents the type of binary sub-cell within which the integration is performed.

The term N_g in Equation (42) represents the minimum loom harness number as defined in Ref. [8]. Every binary sub-cell employed to construct the complete unit-cell of the particular weave occupies N_g unique locations within the domain of the complete unit-cell, which is assembled using $N_g \times N_g$ number of sub-cells. Accordingly, the total volume occupied by the warp tows is computed by summing up the volume of the warp tows calculated for each sub-cell. Therefore the double summation from 1 to N_g over the indices m and n appears in Equation (42).

In a non-dimensional environment the local binary sub-cell coordinate system is subject to the following coordinate transformation:

$$\hat{x} = \frac{x}{a} \quad \hat{y} = \frac{y}{a}$$

Incorporating the normalization of the geometry parameters discussed in an earlier section, the above coordinate transformation and substituting $V_{\text{total}} = 2ba^2$, the volume fraction of the warp bundles, v_{warp} , is computed as:

$$v_{\text{warp}} = \sum_{m=1}^{N_g} \sum_{n=1}^{N_g} \left[\int_{-\hat{a}_i/2}^{\hat{a}_i/2} \int_{-\hat{a}_i/2}^{\hat{a}_i/2} \frac{\{s_w^t(i, a\hat{x}, a\hat{y}) - s_w^b(i, a\hat{x}, a\hat{y})\}}{2b} d\hat{y} d\hat{x} \right] \quad (43)$$

In the above equation the ($\hat{\quad}$) symbol denotes non-dimensional quantities.

The tow surface functions developed earlier and reported in Table 3 are linear functions of the bundle height b . Therefore, when the surface functions representing the warp tows in different binary sub-cells are substituted into Equation (43), the parameter \hat{b} appears as a common factor in the functions $s_w^t(i, a\hat{x}, a\hat{y})$ and $s_w^b(i, a\hat{x}, a\hat{y})$. Therefore, the parameter \hat{b} is cancelled as it appears exactly once in the numerator and the denominator. Consequently, the volume fraction of the warp tows as given by Equation (43) is not a function of \hat{b} and hence of \hat{h} (for $\hat{h} = 2\hat{b}$), but does vary with changing g/a ratios [1,15]. In balanced satin weave fabrics, the volume occupied by the fill tows is equal to the volume occupied by the warp tows ($V_{\text{fill}} = V_{\text{warp}}$), and hence the matrix volume fraction in the porous matrix model is given by $v_{\text{matrix}} = (1 - 2v_{\text{warp}})$.

In the case of PW fabrics, the warp tow volume fraction is simply computed as [1,15]:

$$v_{\text{warp}} = \int_{-1/2}^{1/2} \int_{-1/2}^{1/2} \frac{\{s_w^t(a\hat{x}, a\hat{y}) - s_w^b(a\hat{x}, a\hat{y})\}}{2b} d\hat{y} d\hat{x} \quad (44)$$

where $s_w^t(a\hat{x}, a\hat{y})$ and $s_w^b(a\hat{x}, a\hat{y})$ are the normalized top and bottom surface functions of the warp tow layer in the PW system as discussed in Ref. [1].

In Figure 18, the change in the volume fraction of the polymer matrix material in the porous matrix model of the PW, 4HS, 5HS, and 8HS satin weave fabrics is monitored.

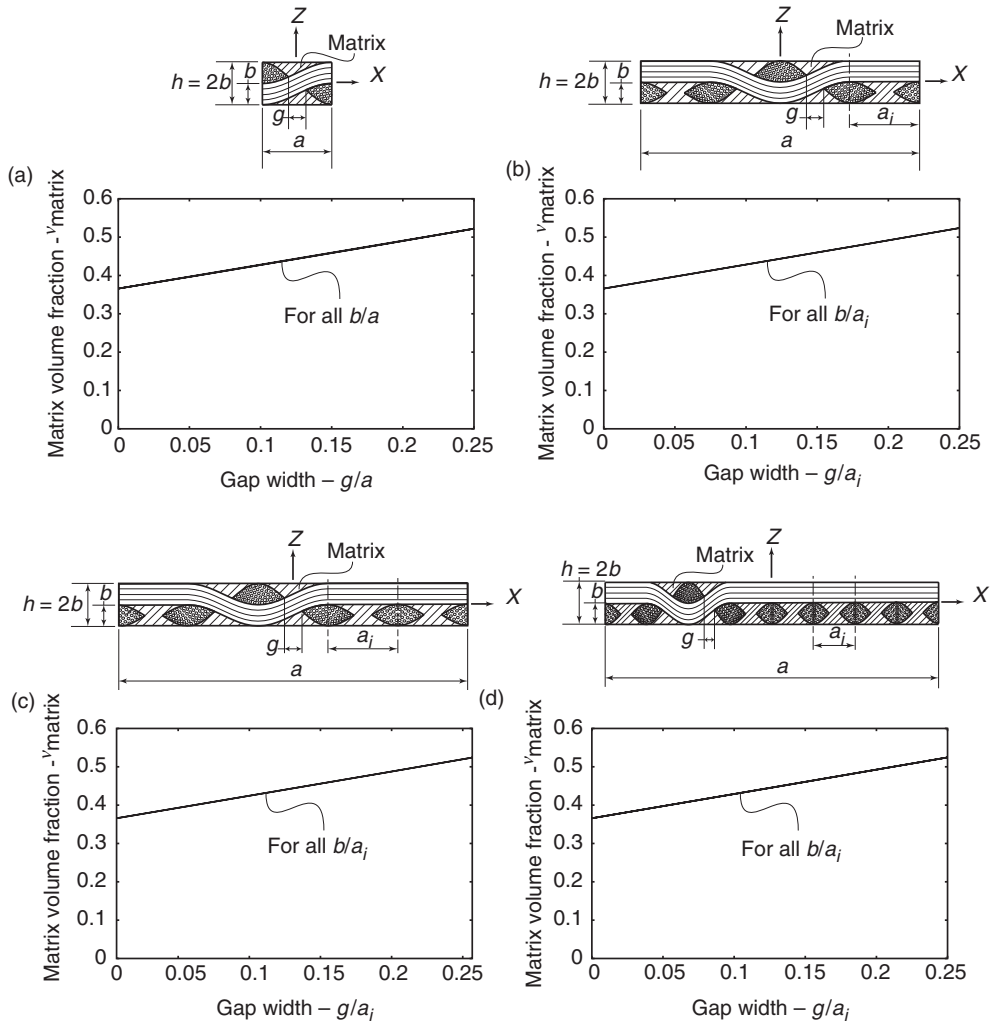


Figure 18. Inter-tow matrix volume fraction in the porous matrix model computed as a function of increasing inter-tow gap length. In all of the above simulations $v_f = v_w = (1 - 2v_m)$. (a) Matrix volume fraction in the PW composite. (b) Matrix volume fraction in the 4HS composite. (c) Matrix volume fraction in the 5HS composite. (d) Matrix volume fraction in the 8HS composite.

The normalized tow thickness $\hat{b} = b/a$ in the PW fabric while $\hat{b} = b/a = (a_i/a)(b/a_i) = \hat{a}_i \hat{b}_i$ in the case of 4HS, 5HS, and 8HS satin weave fabric composites, as discussed in the previous section. For the PW system $\hat{b} = 0.2$ whereas for the 4HS, 5HS, and 8HS woven systems $\hat{b}_i = b/a_i = 0.2$. Note that a_i for the individual satin weave fabrics is computed with the aid of Equation (35). The plain weave as well as the satin weaves are considered to be balanced fabrics with equal number of fibers in the warp and fill tows. The gap between parallel tows is varied in the range of $0 \leq g/a \leq 0.2$ in the plain weave fabric, while the gap between parallel tows is varied in the range of $0 \leq g/a_i \leq 0.2$ in the satin weave fabrics. The results presented in Figure 18 predict that the matrix volume fraction is independent of the tow thickness \hat{b} as a result of which, the computed values of v_{matrix} are identical for

all b/a in the PW system and for all b/a_i in the satin weave morphologies. Expectedly, the results in Figure 18 report an increasing trend in v_{matrix} as either the ratio g/a in the plain weave system or the ratio g/a_i in the satin weave fabrics is increased.

It may be of importance to observe that the inter-tow matrix volume fraction for the 8HS systems varies between 0.38 to 0.52. One would expect that for high harness systems indeed the matrix volume fraction approaches that calculated for an equivalent cross-ply laminate. In such a case one would expect the respective matrix volume fraction to be approximately 50% which is encompassed by the predictions reported in Figure 18.

The volume fraction of the fiber tows in the layered matrix model is identical to the volume fraction of the tows in the corresponding porous matrix model. However, in the layered matrix model, the sum of the volume occupied by the matrix material and the large macroscopic voids is equal to the volume occupied by the matrix material in the porous matrix model. As such, the volume fraction of the matrix material in the layered matrix model is both a function of t/a_i and b/a_i as well as g/a_i in satin weave fabrics. Whereas in the PW fabric, the volume fraction of the matrix material in the layered matrix model is a function of t/a , b/a , as well as g/a . Following the methodology developed earlier to compute the volume fraction of the fiber tows in satin weave fabric composites, the volume fraction of the matrix material in satin weave ceramic–matrix composites characterized by a network of inter-connected macroscopic matrix voids is computed as:

$$v_{\text{matrix}} = \sum_{m=1}^{N_g} \sum_{m=1}^{N_g} \left[\int_{-\hat{a}_i/2}^{\hat{a}_i/2} \int_{-\hat{a}_i/2}^{\hat{a}_i/2} \frac{\left\{ \begin{array}{l} (s_{um}^t(i, a\hat{x}, a\hat{y}) - s_{um}^b(i, a\hat{x}, a\hat{y})) + \\ (s_{mm}^t(i, a\hat{x}, a\hat{y}) - s_{mm}^b(i, a\hat{x}, a\hat{y})) + \\ (s_{lm}^t(i, a\hat{x}, a\hat{y}) - s_{lm}^b(i, a\hat{x}, a\hat{y})) \end{array} \right\}}{2b} d\hat{y} d\hat{x} \right] \quad (45)$$

while the volume fraction of the matrix material in the PW fabric composite is computed as:

$$v_{\text{matrix}} = 2 \int_{-1/2}^{1/2} \int_{-1/2}^{1/2} \frac{\{s_{um}^t(a\hat{x}, a\hat{y}) - s_{um}^b(a\hat{x}, a\hat{y})\}}{2b} d\hat{y} d\hat{x} \quad (46)$$

where $s_{um}^t(a\hat{x}, a\hat{y})$ and $s_{um}^b(a\hat{x}, a\hat{y})$ are the normalized top and bottom surface functions of the upper matrix layer in the PW system as discussed in Ref. [1].

When the relevant expressions for the matrix surface functions are substituted into Equations (45) and (46), the parameter \hat{b} in Equations (45) and (46) will not be eliminated due to the inherent discontinuous nature of these functions. The variation in the matrix volume fraction is plotted for changing t/a and fixed $b/a = 0.15$ at three different values of g/a for the PW morphology as shown in Figure 19(a). As expected, the matrix volume fraction $v_{\text{matrix}} = 0.0$ for $t/a = 0.0$ and increases with increasing t/a . If $g/a < 2b/a$, then the central hole is filled with matrix material as $t/a \rightarrow b/a$ and the matrix volume fraction asymptotes to that of the porous matrix model. The matrix volume fraction is monitored for changing values of b/a in Figure 20(a) for the PW fabric. The non-dimensional matrix thickness expressed as the geometry parameter t/a is kept fixed at 0.05, while the matrix volume fraction is plotted for varying b/a for three different values of g/a . Since t/a is fixed, the total volume occupied by the matrix material within the unit-cell remains constant, but

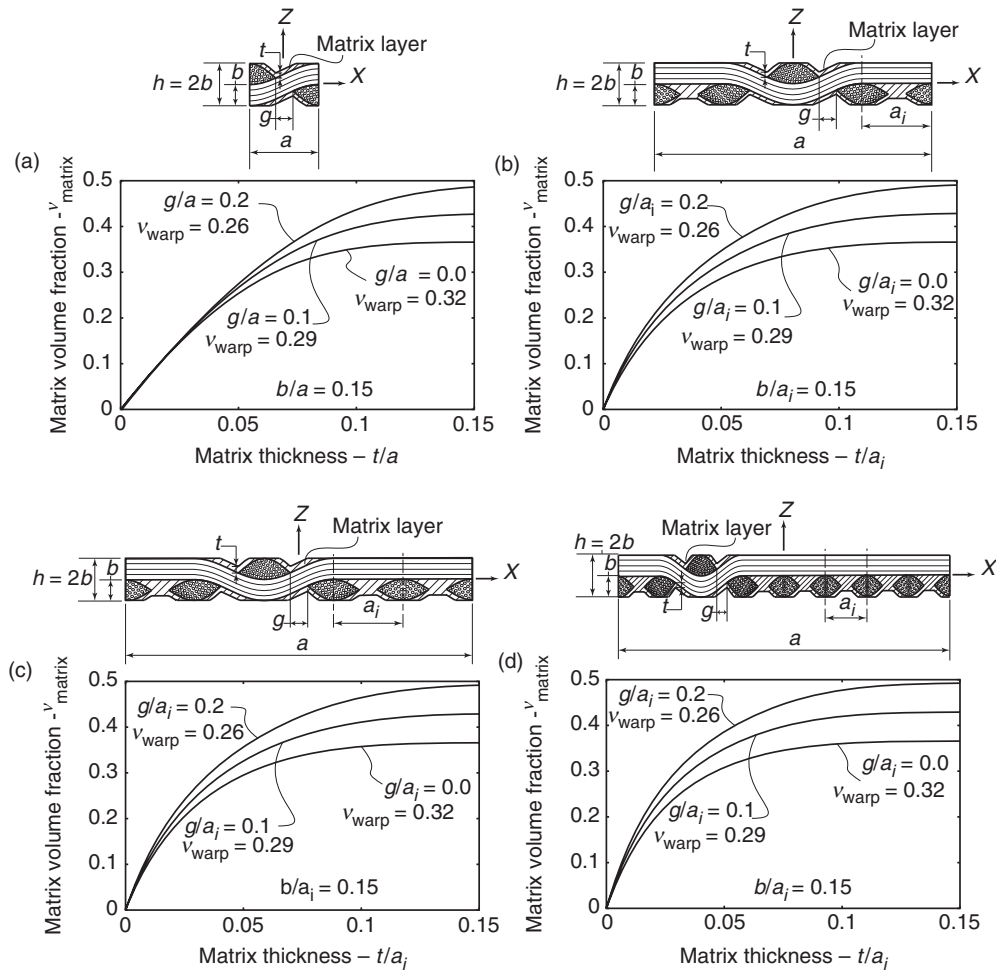


Figure 19. Inter-tow matrix volume fraction in the layered matrix model computed as a function of increasing matrix thickness. The void volume fraction in all of the above simulations is computed as $v_{void} = 1 - (v_m + 2v_w)$. (a) Matrix volume fraction in the PW composite. (b) Matrix volume fraction in the 4HS composite. (c) Matrix volume fraction in the 5HS composite. (d) Matrix volume fraction in the 8HS composite.

the volume of the unit-cell itself increases with increasing b/a , resulting in decreasing matrix volume fraction and increasing void volume fraction. As $b/a \rightarrow 0$, the matrix volume fraction reaches steady-state values for different g/a ratios. This is because t/a is fixed and for small b/a , $t/a \rightarrow h/a$ thus tending to become identical to the porous matrix model.

While the results reported in Figures 19(a) and 20(a) pertain specifically to the PW system, similar results are reported for the 4HS, 5HS, and 8HS satin weaves for increasing t/a_i and b/a_i under three different inter-tow gap lengths $g/a_i = 0.0, 0.1, \text{ and } 0.2$ in Figures 19(b) (c), (d), and 20(b), (c), (d), respectively. The tow volume fractions in the PW, 4HS, 5HS, and 8HS woven systems remain the same for each b/a_i but the matrix volume fraction in the satin weaves increases due to the additional middle matrix layer. In other words, for given values of the inter-tow gap g/a_i , tow thickness b/a_i and matrix thickness t/a_i , the matrix volume fraction in satin weave fabric composites is shown

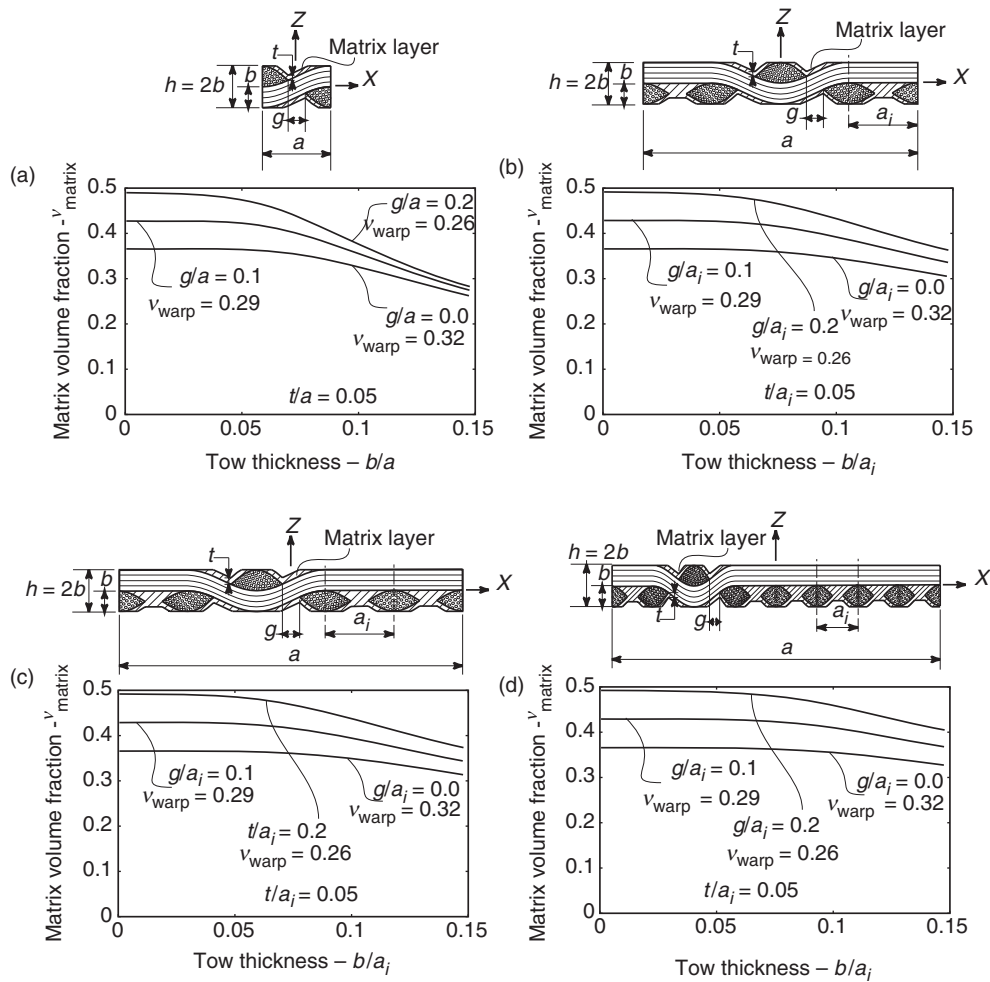


Figure 20. Inter-tow matrix volume fraction in the layered matrix model computed as a function of increasing tow height. Consistent with the studies reported in Figure 19, the void volume fraction in all of the above simulations is computed as $v_{void} = 1 - (v_m + 2v_w)$. (a) Matrix volume fraction in the PW composite. (b) Matrix volume fraction in the 4HS composite. (c) Matrix volume fraction in the 5HS composite. (d) Matrix volume fraction in the 8HS composite.

to be greater than the matrix volume fraction in the corresponding PW system, as reported in Figure 19 and 20. Therefore, the void volume fraction in satin weave fabric ceramic–matrix composites (CMCs) fabricated via the CVI technique is less than corresponding plain weave CMCs fabricated via the same CVI technique.

DISCUSSION

The methodology of modeling woven composites as stacked non-uniform individual layers first developed by Kuhn and Charalambides [1] has greatly reduced the complexity in characterizing their geometry and the formulation of reliable analysis tools.

The general ideas presented in Ref. [1] have been extended in this work to model the complicated satin weave fabrics using a sub-domain approach [2]. Focusing the mathematical treatment of the fiber tow and matrix layers on one such sub-domain and then using the surface expressions so developed to model other unique sub-domains lends easily to the computer implementation of the general algorithm described in an earlier section. The mathematical surface functions developed in this study are of the general class developed in Ref. [1] and accurately model the complex micro-structural architecture of satin weave composites. The surface functions are able to capture the unique characteristics of both the polymer and ceramic–matrix materials deposited onto the woven fiber bundles through the CVI technique.

It may be of importance to emphasize that the geometry models developed as part of this study are expected to yield improved estimates of the spatially varying deformation, strain and stress fields dominating this complex class of composite systems. Prior models such as those reported in Ref. [8] utilized simplistic geometry approximation for the bundle phases. As a result, naturally inadmissible strain and stress discontinuity are introduced thus limiting the model capabilities in predicting the requisite strain and stress fields. The current model, as demonstrated elsewhere [12,18,22–24] possess the critical geometry and material definition required for the prediction of more accurate mechanical fields. This is an important distinction, especially when micro-fields derived through the models are used to drive the evolution of micro-damage and eventual composite fracture.

As such, the geometry models developed herein could now be employed to formulate fundamental elasticity boundary value problems aimed at addressing the mechanical and thermal response of the satin and plain weave PMCs and CMCs. The fiber tow and matrix layer surface functions developed herein may be extended to model hybrid fabrics incorporating different numbers of fibers in the fill and warp directions. This type of modeling effort is addressed in Ref. [25].

The example finite element meshes presented in Figure 17 were discretized using eight-noded linear continuum brick elements. Due to the weave geometry and undulations of the fiber tows, some elements, especially in the *middle matrix layer* tend to be very slender. Such a situation may result in erroneous stress estimates in those limited regions. As a means of avoiding the above, and before finalizing each mesh for a production run, element quality checks were performed using tools integrated into the meshing algorithms as well as other external tools available in commercial software such as Ref. [26]. The above checks indicated that in the range of $0.05 \leq \hat{b}_i \leq 0.2$, and $0.0 \leq \hat{g}_i \leq 0.2$, representative of most woven systems, six eight-noded elements across the tow width, two elements each in the tow and *lower, middle* and *upper* matrix thickness directions, and across the gap region, in PMCs yield acceptable results. While for CMCs as well the above element densities were determined to be acceptable, the discrete voids in these materials were required to be discretized with at least three rings of elements with 16 elements per ring, in order to accurately capture local stress concentrations.

CONCLUSIONS

In this study, 3D geometry models of the complex micro-structural architecture of satin weave CMCs comprised of discrete macroscopic porosity have been developed. The individual material micro-constituents were treated as non-uniform layers in order to describe their spatial variation mathematically. The fiber tows were modeled as

non-uniform warp and fill tow layers while the matrix material was partitioned into the *upper matrix*, *middle matrix* and the *lower matrix* layers enabling the robustness and efficient matrix geometry description.

Mathematical surface functions describing the geometry of these individual layers within the domain of binary sub-cells were developed. These functions are rather general in nature and can be employed to study a broad range of satin weave composite systems. The porous matrix model was developed to simulate the micro-structure associated with satin and plain woven PMCs. The domain outside of the fiber tows in such materials is completely occupied by the *soft*-polymer matrix material, which may exhibit dispersed porosity. On the other hand, the layered matrix model was developed to study the fiber tow architecture and matrix material deposition via the CVI technique in satin and plain woven CMCs. The *stiff*-ceramic–matrix material is deposited as a thin layer of spatially varying thickness over the fiber tows in woven CMCs. CMCs fabricated via the CVI technique have been known to possess large-scale discrete porosity [19,21]. The mathematical functions developed in this work are able to accurately capture such intricate geometric details of the micro-structural architecture of woven CMCs.

The woven unit-cell geometry models developed in this work were employed to perform parametric studies as needed to establish the micro-constituent volume fraction functional relationships, in both PMC and CMC systems. The results presented for the PW architecture are in excellent agreement with similar studies reported in Ref. [1], while the trends in the matrix volume fraction as a function of different geometry parameters appear to follow intuitive trends.

The geometry models and associated 3D finite element meshes were developed as the first critical step of a comprehensive numerical study aimed at capturing the linear and damage induced non-linear response of woven systems. Related mechanics models and model predictions are presented elsewhere [12].

ACKNOWLEDGMENTS

Support for this study was provided by Technology Assessment and Transfer (TAT) and Ceramic Composites, Inc. (CCI) through an STTR–US Air Force subcontract.

REFERENCES

1. Kuhn, J.L. and Charalambides, P.G. (1999). Modeling of Plain Weave Fabric Composite Geometry, *Journal of Composite Materials*, **33**(3): 188–220.
2. Hewitt, J.A., Brown, D. and Clarke, R.B. (1995). Computer Modelling of Woven Composite Materials, *Composites*, **26**(2): 134–140.
3. Morscher, G.N. (2006). Modeling the Elastic Modulus of 2D Woven CVI SiC Composites, *Composite Science and Technology*, **66**: 2804–2814.
4. Glaessgen, E.H., Pasotre, C.M., Griffin, H. and Birger, A. (1996). Geometrical and Finite Element Modelling of Textile Composites, *Composites: Part B*, **27B**(1): 43–50.
5. Naik, R.A. (1994). Analysis of Woven and Braided Fabric Reinforced Composites, Technical report, NASA, June.
6. Vandeurzen, Ph., Ivens, J. and Verpoest, I. (1996). A Three-Dimensional Micromechanical Analysis of Woven-Fabric Composites: I. Geometric Analysis, *Composites Science and Technology*, **56**: 1303–1315.

7. Vandeurzen, Ph., Ivens, J. and Verpoest, I. (1996). A Three-Dimensional Micromechanical Analysis of Woven-Fabric Composites: II. Elastic Analysis, *Composites Science and Technology*, **56**: 1317–1327.
8. Raju, I.S. and Wang, J.T. (1994). Classical Laminate Theory Models for Woven Fabric Composites, *Journal of Composites Technology and Research*, **16**(4): 289–303.
9. Cox, B.N. and Flanagan, G. (1997). Handbook of Analytical Methods for Textile Composites, Technical report, NASA, March.
10. Ishikawa, T. and Chou, T.-W. (1983). One-Dimensional Micromechanical Analysis of Woven Fabric Composites, *AIAA Journal*, **21**(12): 1714–1721.
11. Ishikawa, T. and Chou, T.-W. (1982). Stiffness and Strength Behavior of Woven Fabric Composites, *J. Materials Science*, **17**: 3211–3220.
12. Madhwapati Prabhakar Rao. (2005). *Modeling the Thermo-Mechanical Elastic Response of Plain and Satin Weave Composites*, PhD thesis, The University of Maryland.
13. Whitcomb, J.D., Chapman, C.D. and Tang, X. (2000). Derivation of Boundary Conditions for Micromechanics Analyses of Plain and Satin Weave Composites, *Journal of Composite Materials*, **34**(9): 724–746.
14. Whitcomb, J.D. and Tang, X. (2001). Effective Moduli of Woven Composites, *Journal of Composite Materials*, **35**(23): 2127–2144.
15. Kuhn, J.L. (1998). *Mechanical Behavior of Woven Ceramic Matrix Composites*, PhD thesis, The University of Maryland.
16. Haan, S.I. (2000). *Modeling of the Mechanical Response of Plain Weave Composites*, PhD thesis, The University of Maryland.
17. Kuhn, J.L., Haan, S.I. and Charalambides, P.G. (2000). Stress Induced Matrix Microcracking in Brittle Matrix Plain Weave Fabric Composites Under Uniaxial Tension, *Journal of Composite Materials*, **34**(19): 1640–1664.
18. Rao, M.P., Pantiuk, M. and Charalambides, P.G. (2004). Initiation of Matrix Cracking in Woven Ceramic Matrix Composites, *Ceramic Transactions X. Proceedings of the 106th Annual General Meeting and Exposition of the American Ceramic Society*, 165–180.
19. Patterson, M.C.L. (2002). Private Communication. Advanced Ceramics Research, 3292 East Hemisphere Loop, Tucson, AZ 85706.
20. Morscher, G.N. (2004). Stress-dependent matrix cracking in 2D woven SiC-fiber reinforced melt-infiltrated SiC matrix composites, *Composites Science And Technology*, **64**: 1311–1319.
21. Morscher, G.N. (2004). Private Communication. NASA Glen Research Center, Ohio Space Institute, Lewis Field, MS-106-5, Cleveland, OH 44135, USA.
22. Kuhn, J.L. and Charalambides, P.G. (1998). Elastic Response of Porous Matrix Plain Weave Fabric Composites: Part I-Modeling, *Journal of Composite Materials*, **32**(16):1426–1471.
23. Kuhn, J.L. and Charalambides, P.G. (1998). Elastic Response of Porous Matrix Plain Weave Fabric Composites: Part II-Results, *Journal of Composite Materials*, **32**(16): 1472–1507.
24. Haan, S.I., Charalambides, P.G., Kuhn, J.L. and Patterson, M.C.L. (2003). Supercritical matrix microcracking in brittle matrix plain weave composites under uniaxial tension, *Mechanics of Materials*, **35**(12): 1107–1126.
25. Rao, M.P., Pantiuk, M. and Charalambides, P.G. (2008). Micro-Mechanical Modeling of C_f/C Ion Propulsion Grids (In progress).
26. Hibbit, Karlsson and Sorensen, Inc. (2004). *ABAQUS/Standard Version 6.5-1*.